

A GENERAL APPROACH TO ENHANCE SLOPE LIMITERS ON NON-UNIFORM GRIDS

XIANYI ZENG*

Abstract. A general approach to study and enhance the slope limiter functions on non-uniform grids is presented. Slope limiters are preferred in high-resolutions schemes in general and MUSCL in particular to solve hyperbolic conservation laws. However, most 1D limiters are developed assuming uniform meshes in space, which are shown to be inadequate on non-uniform grids. Especially, second-order convergence is shown to be lost when the conventional limiters are applied on irregular grids in the case of smooth solutions. A methodology based on the classical reconstruct-evolve-project approach and Harten's stability theory is presented to study the slope limiters on 1D non-uniform computational grids. Sufficient conditions for the limiters to lead to formal second-order spatial accuracy, total-variational-diminishing stability and symmetry-preserving property are derived. The analysis and results extend naturally to cell-centered finite volume methods in multiple dimensions. Several most widely used conventional limiters are enhanced to satisfy these conditions, and their performances are illustrated by various 1D and 2D numerical examples.

Key words. non-uniform grid, MUSCL, slope limiter, TVD, symmetry-preserving

AMS subject classifications. 65M06,65M08,65M12,35L65

1. Introduction. Limiting strategies are often employed in high-resolution finite volume methods (FVM) to solve scientific and engineering problems that are governed by time-dependent hyperbolic conservation laws (HCL). These problems are usually characterized by discontinuous solutions at finite time even though the initial conditions are smooth. In practice, two classes of limiting techniques are often employed: flux limiting, exemplified by Flux-Corrected Transport (FCT) methods [3, 27, 5]; and slope limiting, like the Monotone Upstream-centered Schemes for Conservation Laws (MUSCL) schemes [23, 13, 4, 10]. Both techniques try to keep the numerical scheme high-order accurate (often second-order) everywhere in the computational domain except near discontinuities, where order of accuracy is lowered to first-order in space to achieve certain stability property, like total variational diminishing (TVD); and they are equivalent to each other in certain situations. This paper focuses on slope limiters, but the latter are also reformulated in the analysis part of the paper as equivalent flux limiters to provide better insight of their functionalities.

Despite their wide acceptance in practical computation, the most widely used slope limiters are developed in the context of 1D uniform meshes. These limiters are applied to solve problems in multiple dimensions by: (1) dimension-splitting on structured meshes, or (2) solving a local directional 1D problem on unstructured meshes. On the other hand, the limitations of these conventional limiters are well documented in literature [24, 2]. V. Venkatakrishnan [24] noticed that non-smooth limiter functions led to non-converging solutions when considering steady problems. Thus smoothness of the limiter functions is desired in practical computations. M. Berger et. al. [2] reformulated the slope limiters in a symmetric form other than the classical one, and studied their effects on non-uniform grids. In this report, conventional limiters are shown to lead to less than second-order accuracy on non-uniform grids; and several modified limiter functions, including two modified *van Leer* limiters, are provided. However, the proposed generalized *van Leer* limiters therein

*Postdoctoral associate, Department of Civil and Environmental Engineering, Duke University, Durham, North Carolina 27708 (xy.zeng@duke.edu).

lose the C^∞ property that is possessed by the conventional one; in addition, no generalization to the popular *van Albada* limiter is provided.

In this paper, a different approach is taken to analyze the functionality of limiter functions when non-uniform grids are employed in computation. This approach modifies the original reconstruct-evolve-project (REP) procedure [7] to take into account of the irregularity of the computational grids; and it requires no reformulation of the variables (cf. [2]). The analysis focuses applying MUSCL scheme to 1D problems on non-uniform grids, in which case sufficient conditions are derived for designing the limiter functions such that TVD stability and formal second-order accuracy in space are achieved. In addition, symmetry-preserving property on non-uniform meshes are formally defined, and a sufficient condition for the limiters to preserve symmetric solutions is provided. The analysis in 1D extends naturally to multiple dimensions for cell-centered FVMs [1, 2]. The reason that it is not suitable for vertex-centered FVMs, for example, the dual-cell approach [1], is that these methods usually compute fluxes at edge centers, which is equivalent to a locally uniform 1D grid.

Several most widely used slope limiters are enhanced to satisfy the derived conditions. The enhancements include novel modifications to the *van Leer* limiter and the *van Albada* limiter, which preserve the C^∞ property of their conventional counterparts. The performance of these enhanced limiters are illustrated by various 1D and 2D numerical examples.

The remainder of the paper is organized as follows. In Section 2, FVM with MUSCL is briefly reviewed and a case study of solving 1D Euler equations on non-uniform grids is presented to raise the issue of concern. Mathematical analysis of applying slope limiters with non-uniform 1D meshes are given in Section 3, where sufficient conditions are derived for designing slope limiter functions such that the resulting schemes are TVD stable, second-order accurate in space and preserve symmetric solutions. Several most widely used limiter functions are enhanced to satisfy these conditions, and they are given in Section 4. This section also shows by a case study of the *van Leer* limiter, which explains why present research is important. The performance of the enhanced limiters is evaluated by numerical examples in Section 5. Finally Section 6 concludes the paper.

2. Case study.

2.1. The MUSCL scheme. Consider the MUSCL scheme [23] that is applied to solve the general 1D scalar conservation law

$$u_t + f(u)_x = 0 \quad (2.1)$$

In typical FVM, the 1D computational domain Ω is divided into non-overlapping cells $\Omega_i = [x_{i-1/2}, x_{i+1/2}]$, where $\dots < x_{i-1/2} < x_{i+1/2} < x_{i+3/2} < \dots$ are cell faces. The cell center of Ω_i is defined by $x_i = \frac{1}{2}(x_{i-1/2} + x_{i+1/2})$, and $\Delta x_i := |\Omega_i| = x_{i+1/2} - x_{i-1/2}$ is the size of the cell. The mesh is supposed to be fixed in time.

In the remaining of the paper, the following notations are used: $u(x, t)$ denotes the exact solution of the PDE of a generic variable u ; $\bar{u}_i(t)$ designates the exact cell-averaged data at time-instance t over the cell Ω_i ; u_i^n designates the numerical approximation of the value $\bar{u}_i(t^n)$; and finally u_i denotes the semi-discretized approximation of \bar{u}_i .

Integrating Eq. (2.1) in space over Ω_i one obtains

$$\frac{d\bar{u}_i(t)}{dt} + \frac{f(u(x_{i+1/2}, t)) - f(u(x_{i-1/2}, t))}{\Delta x_i} = 0 \quad (2.2)$$

where $\bar{u}_i(t)$ is defined by

$$\bar{u}_i(t) = \frac{1}{\Delta x_i} \int_{x_{i-1/2}}^{x_{i+1/2}} u(x, t) dx \quad (2.3)$$

Eq. (2.2) leads to the semi-discretized equations for the approximated solution u_i

$$\frac{du_i}{dt} + \frac{F_{i+1/2} - F_{i-1/2}}{\Delta x_i} = 0 \quad (2.4)$$

Here $F_{i+1/2}$ is the numerical flux approximating $f(u(x_{i+1/2}, t))$; and it is calculated using the semi-discrete solutions u_k . The canonical Godunov scheme [6] defines the numerical flux $F_{i+1/2}$ as the solution of the Riemann problem defined by left data u_i and right data u_{i+1}

$$F_{i+1/2}^{Godunov} = F^{Riem}(u_i, u_{i+1})$$

Whereas due to the high computational cost of the exact Riemann solutions, F^{Riem} is often replaced by more economical approximate Riemann solvers, for example, the Roe solver [14] F^{Roe} .

The spatial approximation $F_{i+1/2} = F^{Roe}(u_i, u_{i+1})$ leads to first-order error in space, and a second-order extension is to linearly reconstruct the state vector to the left and to the right of the cell face $x_{i+1/2}$

$$F_{i+1/2} = F^{Roe}(u_i + \frac{1}{2}\sigma_i\Delta x_i, u_{i+1} - \frac{1}{2}\sigma_{i+1}\Delta x_{i+1}) \quad (2.5)$$

where $\sigma_{i,i+1}$ are the slopes for the linear reconstruction in $\Omega_{i,i+1}$. In order that Eq. (2.5) gives rise to a second-order accurate discretization in space, σ_i should be consistent with the local gradients u_x at the cell centers x_i [13], denoted by $D_x u_i$. One of the most natural choices for σ_i on uniform meshes is given by

$$\sigma_i = D_x^+ u_i := \frac{1}{\Delta x_i}(u_{i+1} - u_i) \quad (2.6)$$

To avoid spurious oscillations near discontinuities caused by Eq. (2.6), the MUSCL approach multiplies $D_x u_i$ with a restricting factor ϕ , called slope limiter

$$\sigma_i = \phi_i D_x u_i \quad (2.7)$$

Here and in the remains of the paper, the symbol ϕ is reserved for slope limiters.

Once the limited slopes σ_i are computed, one use any preferred ODE solver, like forward Euler (for simplicity of analysis), to discretize Eq. (2.4) in time

$$\frac{u_i^{n+1} - u_i^n}{\Delta t} + \frac{F_{i+1/2}^n - F_{i-1/2}^n}{\Delta x_i} = 0 \quad (2.8)$$

Integrating Eq. (2.2) over the time interval $[t^n, t^{n+1}]$ one has the exact integral form of (2.1)

$$\begin{aligned} \frac{\bar{u}_i(t^{n+1}) - \bar{u}_i(t^n)}{\Delta t^n} + \frac{1}{\Delta x_i} \left(\frac{1}{\Delta t^n} \int_{t^n}^{t^{n+1}} f(u(x_{i+1/2}, t)) dt \right. \\ \left. - \frac{1}{\Delta t^n} \int_{t^n}^{t^{n+1}} f(u(x_{i-1/2}, t)) dt \right) = 0 \end{aligned} \quad (2.9)$$

where $\Delta t^n = t^{n+1} - t^n$. It is clear that the numerical flux $F_{i+1/2}^n$ represents an approximation to the time-averaged flux at the cell face

$$F_{i+1/2}^n \approx \frac{1}{\Delta t^n} \int_{t^n}^{t^{n+1}} f(u(x_{i+1/2}, t)) dt \quad (2.10)$$

2.2. Slope limiters. In practice, ϕ_i in Eq. (2.6) is a function of a local smoothness monitor θ_i , of which a popular choice [20, 2] is given by

$$\theta_i = \frac{u_i - u_{i-1}}{u_{i+1} - u_i} \quad (2.11)$$

this is the default smoothness monitors throughout the paper unless otherwise mentioned. Conventional practice of MUSCL defines the limiters ϕ_i as

$$\phi_i = \phi(\theta_i) \quad (2.12)$$

And the absence of the subscript of ϕ in the right hand side of Eq. (2.12) highlights the common strategy that a uniform limiter function is applied everywhere in the computational domain. A. Harten [9] showed on uniform meshes, a sufficient condition for the fully discretized system Eq. (2.8) to be TVD stable is

$$0 \leq \phi(\theta) \leq 2, \quad 0 \leq \frac{\phi(\theta)}{\theta} \leq 2, \quad \forall \theta \in \mathbb{R} \quad (2.13)$$

On the other hand, the effectiveness of limiters in retaining formal high-order accuracy when the solutions are smooth can be studied by rewriting Eq. (2.5) in the flux-corrected form

$$F(u_i + \frac{1}{2}\sigma_i\Delta x_i, u_{i+1} - \frac{1}{2}\sigma_{i+1}\Delta x_{i+1}) = F_{i+1/2}^L + \varphi_{i+1/2} (F_{i+1/2}^H - F_{i+1/2}^L) \quad (2.14)$$

Here F^L is any first-order numerical flux $F_{i+1/2}^L = F(u_i, u_{i+1})$, obtained from an exact or approximated Riemann solver; and F^H designates a high-order flux. The multiplier φ defined at the cell face $x_{i+1/2}$ is thusly a switch between the high-order flux and the low-order flux, and hence called flux limiter. Typically, $\varphi_{i+1/2}$ is a function of another local smoothness monitor defined at cell faces $\theta_{i+1/2}$

$$\varphi_{i+1/2} = \varphi(\theta_{i+1/2}) \quad (2.15)$$

where the absence of the subscript of φ in the right hand side, again, highlights the practice that the uniform flux limiter is employed everywhere.

In order to preserve high-order spatial accuracy, a sufficient condition is $\varphi_{i+1/2} = 1$ for linear data (linearity preserving); in the case of uniform grids, this condition often reduces to

$$\varphi(1) = 1 \quad (2.16)$$

It can be shown for linear problems that given the smoothness monitor θ_j , one can define $\theta_{i+1/2}$ and F^H properly so that Eq. (2.14) is equivalent to Eq. (2.5). This equivalence provides a convenient tool to study the formal order of accuracy a limiter could deliver, as presented in Section 3.

Several the most widely used limiter functions are listed as follows

$$\text{minmod: } \phi^{\text{minmod}}(\theta) = \max(0, \min(\theta, 1)) \quad (2.17a)$$

$$\text{superbee: } \phi^{\text{superbee}}(\theta) = \max(0, \min(2\theta, 1), \min(\theta, 2)) \quad (2.17b)$$

$$\text{MC: } \phi^{\text{MC}}(\theta) = \max(0, \min(2\theta, \frac{1}{2}(1 + \theta), 2)) \quad (2.17c)$$

$$\text{van Leer: } \phi^{\text{van Leer}}(\theta) = \frac{\theta + |\theta|}{1 + |\theta|} \quad (2.17d)$$

$$\text{van Albada: } \phi^{\text{van Albada}}(\theta) = \frac{\theta + \theta^2}{1 + \theta^2} \quad (2.17e)$$

All the five limiter functions satisfy the conditions given by Eq. (2.13) and Eq. (2.16). Among the five, the *minmod* [15], *superbee* [15], *monotonized central* (MC) [22] are piecewise linear; and the *van Leer* limiter [21] and the *van Albada* limiter [19] are smooth functions of the smoothness monitor.

2.3. Loss of accuracy. The case study is to solve the 1D Euler equations with periodic boundary conditions

$$\mathbf{w}_t + \mathbf{f}(\mathbf{w})_x = 0, \quad \mathbf{w} = \begin{bmatrix} \rho \\ \rho u \\ E \end{bmatrix}, \quad \mathbf{f}(\mathbf{w}) = \begin{bmatrix} \rho u \\ \rho u^2 + p \\ u(E + p) \end{bmatrix}, \quad x \in [-1, 1] \quad (2.18)$$

\mathbf{w} is the conservative fluid state vector and \mathbf{f} is the physical flux function. ρ , u and p are density, velocity and pressure respectively; E is the total energy per unit volume

$$E = \rho e + \frac{1}{2} \rho u^2, \quad e = \frac{p}{(\gamma - 1)\rho}, \quad \gamma = 1.4$$

Here e is the specific internal energy and is given by the ideal gas law. The initial condition is the following and also plotted in Figure 2.1.

$$\begin{aligned} \rho(x, 0) &= 1 + 0.5 \sin(\pi x) \\ u(x, 0) &= 2 + 0.5 \sin(\pi x) \\ p(x, 0) &= 1 + 0.5 \sin(\pi x) \end{aligned} \quad (2.19)$$

Both uniform and non-uniform meshes are tested. The uniform mesh has N equal-size cells: $-1 = x_{1/2} < x_{3/2} < \dots < x_{(2N-1)/2} < x_{(2N+1)/2} = 1$. The non-uniform mesh is constructed by perturbing the uniform grid as follows

1. Given N , let $x'_{i+1/2}$, $i = 0, 1, \dots, N$ be the cell faces of the uniform mesh.
2. Set a fixed ratio $r : 0 \leq r < 0.5$.
3. For each inner grid point $x'_{i+1/2}$, $i = 1, \dots, N-1$, define $x_{i+1/2} = x'_{i+1/2} + r\delta_{i+1/2}$ where $\delta_{i+1/2}$ are independent random variables with uniform distribution on $[-h, h]$, $h = 2/N$.
4. The two endpoints are fixed: $x_{1/2} = x'_{1/2}$ and $x_{(2N+1)/2} = x'_{(2N+1)/2}$.

MUSCL with Roe flux and limiter functions in Eqs. (2.17) in space, and second-order TVD Runge-Kutta (TVD RK2) [8] in time are employed in all tests. A CFL number 0.6 is used with the reference cell size $2/N$ for both uniform and non-uniform meshes. This relatively small CFL number is chosen since cell sizes in the non-uniform grids can be smaller than the reference size.

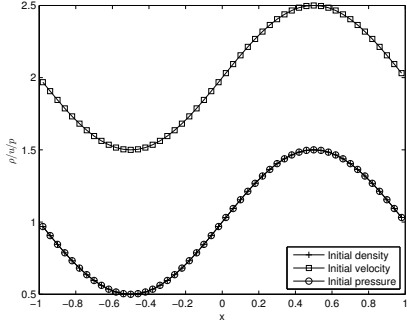


FIG. 2.1. Initial condition for the test problem

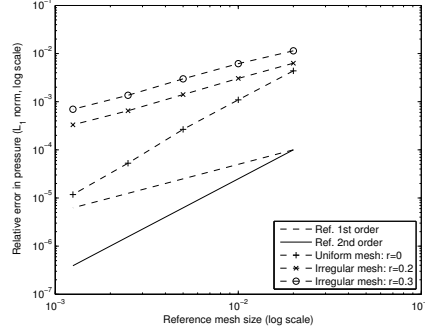


FIG. 2.2. Convergence rates in pressure achieved using van Albada limiters on various meshes

TABLE 2.1

Convergence rates achieved on uniform meshes by applying conventional limiters

	minmod	superbee	MC	van Leer	van Albada
ρ	1.6671	1.9578	2.0036	2.1405	2.2246
u	1.7368	1.6901	2.0703	2.2474	2.2716
p	1.7235	1.8475	2.0067	2.1725	2.3348

Given any limiter function and perturbation ratio r , solutions on five grids with sizes ranging from 100 to 1600 are calculated. The global L_1 errors in pressure calculated with conventional *van Albada* limiter are reported in logarithmic scale in Figure 2.2; and the convergence rates for density, velocity and pressure are reported in Tables 2.1–2.3. The details of calculating the convergence rates, especially on the non-uniform meshes, are offered in Appendix A.

Clearly, second-order convergence is lost when the non-uniform meshes are employed; and the obtained convergence rates are degraded to the first-order. On the other hand, none of the simulations fails (up to $T = 6.0$, see Figure 2.3), indicating stability is still retained. These are exactly the issues this paper concerns.

Remark: practical implementations sometimes involve a switch mechanism that turns on the slope limiter only if discontinuities are detected. Nevertheless, such a strategy falls into the scope of this paper for the following reason. Consider the switch depends on some smoothness monitor θ , which satisfies $\theta = 1$ in the case of linear data. Suppose the switch is turned on if $|\theta - 1| > \delta$ for some small positive number δ ; then given any preferred slope limiter function $\phi(\cdot)$, this switching strategy is equivalent to applying the following limiter

$$\phi_{\text{switch}}(\theta) = \chi_{\{|\theta-1|>\delta\}}\phi(\theta) + \chi_{\{|\theta-1|\leq\delta\}}$$

where χ is the characteristic function. The issues raised in this section equally applies to the slope limiter function ϕ_{switch} .

3. Mathematical analysis.

3.1. Slope limiters and TVD stability. The classical REP approach is applied to study the effectiveness of slope limiters on non-uniform 1D grids to solve the

TABLE 2.2

Convergence rates achieved on non-uniform meshes with $r = 0.2$ by applying conventional limiters

	minmod	superbee	MC	van Leer	van Albada
ρ	1.0993	1.0562	1.0918	1.1426	1.1401
u	1.1186	1.0629	1.0861	1.1425	1.1764
p	1.1051	1.0407	1.0652	1.0915	1.1124

TABLE 2.3

Convergence rates achieved on non-uniform meshes with $r = 0.3$ by applying conventional limiters

	minmod	superbee	MC	van Leer	van Albada
ρ	1.1015	1.0895	1.1190	1.1445	1.1469
u	1.1240	1.0060	1.1293	1.1850	1.1829
p	1.1084	1.0215	1.0812	1.1215	1.1331

model problem given by the 1D scalar advection equation

$$u_t + cu_x = 0 \quad (3.1)$$

where c is a constant. Assuming non-uniform mesh with cell centers denoted by x_i as before, the REP procedure for updating the data from t^n to t^{n+1} is as follows

1. The cell-averaged data u_i^n correspond to t^n from previous time step.
2. (**R**econstruct.) The data are linearly reconstructed on each cell to give the function $\tilde{u}(x, t^n)$ (as illustrated in Figure 3.1 and Figure 3.2)

$$\tilde{u}(x, t^n) = u_i^n + \sigma_i^n(x - x_i), \quad x \in (x_{i-1/2}, x_{i+1/2}) \quad (3.2)$$

3. (**E**volve.) Eq. (3.1) is solved exactly over the time interval $[t^n, t^{n+1}]$ with initial condition given by Eq. (3.2); and the solution is denoted by $\tilde{u}(x, t^{n+1})$ (as illustrated in Figure 3.3).
4. (**P**roject.) Cell-averaged values at time t^{n+1} (Figure 3.4) are calculated as

$$u_i^{n+1} = \frac{1}{\Delta x_i} \int_{x_{i-1/2}}^{x_{i+1/2}} \tilde{u}(x, t^{n+1}) dx \quad (3.3)$$

For general HCL, the “evolve” and “project” steps may be performed approximately.

A classical result concerning the TVD stability is given by Harten:

THEOREM 3.1 (Harten). *If the numerical scheme can be written, for one time step, in the following form:*

$$u_i^{n+1} = u_i^n - C_{i-1}^n(u_i^n - u_{i-1}^n) + D_i^n(u_{i+1}^n - u_i^n) \quad (3.4)$$

Then a sufficient condition for the scheme to be TVD is:

$$\begin{aligned} C_{i-1}^n &\geq 0 \quad \forall i, n \\ D_i^n &\geq 0 \quad \forall i, n \\ C_i^n + D_i^n &\leq 1 \quad \forall i, n \end{aligned} \quad (3.5)$$

here C_i^n , D_i^n can be any numbers including those that are data dependent.

In his original derivations, Harten assumed uniform grids; however this theorem can be

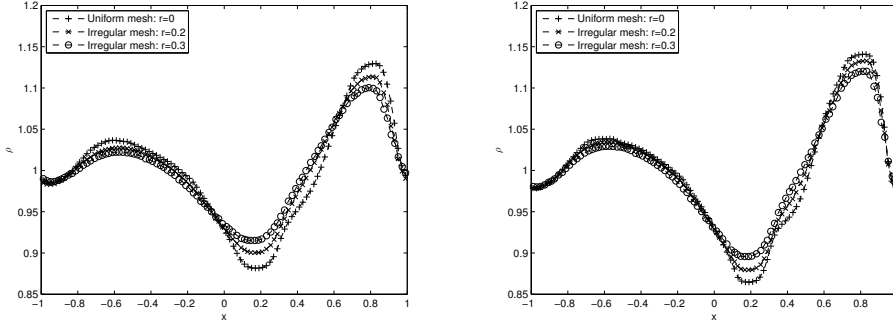


FIG. 2.3. Densities at $T = 6.0$ using minmod limiter (left) and van Albada limiter (right) on uniform and non-uniform meshes

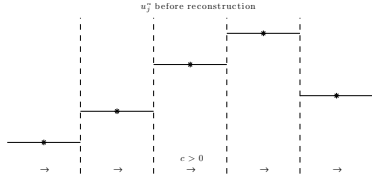


FIG. 3.1. REP-1: Cell-averaged data at t^n

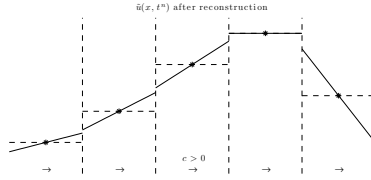


FIG. 3.2. REP-2: Linear reconstruction

applied to non-uniform meshes naturally, by observing that the definition of discrete total variance (Eq. (3.6)) is independent of the particular cell sizes.

$$\text{TV}(\{u_i\}) := \sum_i |u_i - u_{i+1}| \quad (3.6)$$

thus the original proof of Theorem 3.1 carries directly to any 1D grids.

Next, the exact solutions to Eq. (3.1) obtained from Eqs. (3.2)–(3.3) are

$$u_i^{n+1} = u_i^n - \lambda_i(u_i^n - u_{i-1}^n) - \frac{1}{2}\lambda_i[(1 - \lambda_i)\Delta x_i \sigma_i^n - (1 - \lambda_{i-1})\Delta x_{i-1} \sigma_{i-1}^n] \quad (3.7a)$$

if $c > 0$, and

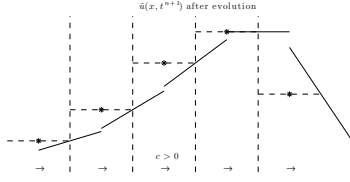
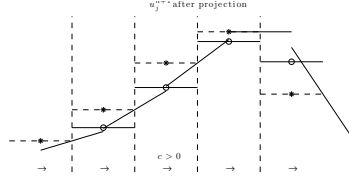
$$u_i^{n+1} = u_i^n - \lambda_i(u_i^n - u_{i+1}^n) + \frac{1}{2}\lambda_i[(1 - \lambda_i)\Delta x_i \sigma_i^n - (1 - \lambda_{i+1})\Delta x_{i+1} \sigma_{i+1}^n] \quad (3.7b)$$

if $c < 0$. Here $\lambda_i = |c\Delta t^n|/\Delta x_i$ is the absolute value of the local Courant number. It is supposed here that $0 \leq \lambda_i \leq 1$. Assuming the smoothness monitor Eq. (2.11) and the approximated gradients Eq. (2.6), the limited slopes are

$$\sigma_i^n = \frac{1}{\Delta x_i} \phi_i(\theta_i)(u_{i+1}^n - u_i^n) \quad (3.8)$$

Note that the limiter function ϕ is equipped with subscript i to allow variance among cells. Plugging Eq. (3.8) into the exact solutions given by Eqs. (3.7), one can choose the parameters C_i^n and D_i^n in Theorem 3.1 as

$$C_{i-1}^n = \lambda_i + \frac{1}{2}\lambda_i(1 - \lambda_i)\frac{\phi_i(\theta_i)}{\theta_i} - \frac{1}{2}\lambda_i(1 - \lambda_{i-1})\phi_{i-1}(\theta_{i-1}), \quad D_i^n = 0 \quad (3.9)$$

FIG. 3.3. REP-3: Solution of Eq. (3.1) at $t = t^{n+1}$ FIG. 3.4. REP-4: Cell-averaged values at $t = t^{n+1}$

if $c > 0$, and:

$$C_{i-1}^n = 0, \quad D_i^n = \lambda_i + \frac{1}{2}\lambda_i(1 - \lambda_i)\phi_i(\theta_i) - \frac{1}{2}\lambda_i(1 - \lambda_{i+1})\frac{\phi_{i+1}(\theta_{i+1})}{\theta_{i+1}} \quad (3.10)$$

if $c < 0$. Then the theorem leads to the conclusion that the REP approach is TVD stable given that

$$\begin{aligned} 0 \leq C_{i-1}^n \leq 1, & \quad \text{if } c > 0 \\ \text{and } 0 \leq D_i^n \leq 1, & \quad \text{if } c < 0 \end{aligned}$$

which are satisfied given that

$$0 \leq \phi_i(\theta) \leq 2, \quad 0 \leq \frac{\phi_i(\theta)}{\theta} \leq 2, \quad \forall i, \theta \quad (3.11)$$

and $0 \leq \lambda_i \leq 1, \forall i$.

Indeed, in the case $c > 0$, assuming the above conditions, one has

$$C_{i-1}^n \geq \lambda_i + \frac{1}{2}\lambda_i(1 - \lambda_i) \cdot 0 - \frac{1}{2}\lambda_i(1 - \lambda_{i-1}) \cdot 2 = \lambda_i \lambda_{i-1} \geq 0$$

and

$$C_{i-1}^n \leq \lambda_i + \frac{1}{2}\lambda_i(1 - \lambda_i) \cdot 2 - \frac{1}{2}\lambda_i(1 - \lambda_{i-1}) \cdot 0 = 2\lambda_i - \lambda_i^2 \leq 1$$

which indicates TVD stability by Theorem 3.1. The proof for $0 \leq D_i^n \leq 1$ in the case $c < 0$ is similar.

To conclude, it is shown that a necessary condition for the limiter functions to lead to TVD stability on non-uniform grids is given by Eqs. (3.11), which are the same as Eqs. (2.13). It thusly explains why TVD stability is retained, even if the conventional slope limiters are applied with non-uniform meshes, as seen in Section 2.

3.2. Second-order spatial accuracy. To investigate the formal spatial order of accuracy of the REP approach, the following fluxes are introduced

$$F_{i+1/2}^n = \begin{cases} cu_i^n + \frac{1}{2}c(1 - \lambda_i)\Delta x_i \sigma_i^n & c > 0 \\ cu_{i+1}^n - \frac{1}{2}c(1 - \lambda_{i+1})\Delta x_{i+1} \sigma_{i+1}^n & c < 0 \end{cases} \quad (3.12)$$

so that the exact solutions given by Eqs. (3.7) is equivalent to those obtained from the finite volume formulation

$$\frac{1}{\Delta t^n} (u_i^{n+1} - u_i^n) + \frac{1}{\Delta x_i} (F_{i+1/2}^n - F_{i-1/2}^n) = 0$$

Plugging the limited slopes (3.8) into Eq. (3.12) leads to

$$F_{i+1/2}^n = cu_i^n + \frac{\phi_i(\theta_i)}{B_{i+1/2}} \left(cu_i^n + \frac{1}{2} B_{i+1/2} c (1 - \lambda_i) (u_{i+1}^n - u_i^n) - cu_i^n \right) \quad (3.13)$$

when $c > 0$, and

$$F_{i+1/2}^n = cu_{i+1}^n + \frac{\phi_{i+1}(\theta_{i+1})}{B_{i+1/2}} \left(cu_{i+1}^n - \frac{1}{2} B_{i+1/2} c (1 - \lambda_{i+1}) (u_{i+2}^n - u_{i+1}^n) - cu_{i+1}^n \right) \quad (3.14)$$

when $c < 0$. Here $B_{i+1/2}$ are coefficients to be determined.

In order to express the fluxes given by Eqs. (3.13)–(3.14) in the flux-corrected form (2.14), the low-order flux F^L and high-order flux F^H need to be defined. In particular, F^L is chosen to be the first-order upwind flux

$$F_{i+1/2}^{L,n} = \begin{cases} cu_i^n & c > 0 \\ cu_{i+1}^n & c < 0 \end{cases} \quad (3.15)$$

and accordingly the high-order fluxes are

$$F_{i+1/2}^{H,n} = \begin{cases} cu_i^n + \frac{1}{2} B_{i+1/2} c \left(1 - \frac{c \Delta t^n}{\Delta x_i} \right) (u_{i+1}^n - u_i^n) & c > 0 \\ cu_{i+1}^n - \frac{1}{2} B_{i+1/2} c \left(1 + \frac{c \Delta t^n}{\Delta x_{i+1}} \right) (u_{i+2}^n - u_{i+1}^n) & c < 0 \end{cases} \quad (3.16)$$

To this end, $B_{i+1/2}$ should be chosen such that the fluxes (3.16) are second-order accurate in space. In the view of Eq. (2.10), and by applying Taylor series expansion in time to evaluate the time-averaged flux in the right hand side of Eq. (2.10)

$$\begin{aligned} \frac{1}{\Delta t^n} \int_{t^n}^{t^{n+1}} cu(x_{j+1/2}, t) dt &= \frac{1}{\Delta t^n} \int_{t^n}^{t^{n+1}} c [u^* + (t - t^n) u_t^*] dt + O((\Delta t^n)^2) \\ &= cu^* + \frac{1}{2} c \Delta t^n u_x^* + O((\Delta t^n)^2) \end{aligned} \quad (3.17)$$

Here the superscript $*$ is used to indicate that the values are evaluated at $(x_{i+1/2}, t^n)$. By feeding the exact data at t^n to the fluxes in Eqs. (3.16), and noticing that $\bar{u}(x_i, t) = u(x_i, t) + O(\Delta x_i^2)$ and $\bar{u}(x_{i+1}, t) = u(x_{i+1}, t) + O(\Delta x_{i+1}^2)$, one obtains

$$\begin{aligned} F_{i+1/2}^{H,n} &= cu^* + \frac{1}{2} cu_x^* \left[\frac{1}{2} B_{i+1/2} \left(1 - \frac{c \Delta t^n}{\Delta x_i} \right) (\Delta x_i + \Delta x_{i+1}) - \Delta x_i \right] \\ &\quad + O(\Delta x_i^2 + \Delta x_{i+1}^2) \end{aligned} \quad (3.18a)$$

if $c > 0$ and

$$\begin{aligned} F_{i+1/2}^{H,n} &= cu^* + \frac{1}{2} cu_x^* \left[-\frac{1}{2} B_{i+1/2} \left(1 + \frac{c \Delta t^n}{\Delta x_{i+1}} \right) (\Delta x_{i+1} + \Delta x_{i+2}) + \Delta x_{i+1} \right] \\ &\quad + O(\Delta x_{i+1}^2 + \Delta x_{i+2}^2) \end{aligned} \quad (3.18b)$$

if $c < 0$. Comparing Eqs. (3.18) and Eq. (3.17), and applying $u_t^* + cu_x^* = 0$, the desired value $B_{i+1/2}$ is

$$B_{i+1/2} = \begin{cases} \frac{2\Delta x_i}{\Delta x_i + \Delta x_{i+1}} & c > 0 \\ \frac{2\Delta x_{i+1}}{\Delta x_{i+1} + \Delta x_{i+2}} & c < 0 \end{cases} \quad (3.19)$$

which leads to the following flux limiters comparing Eq. (2.14) and Eqs. (3.13)–(3.14)

$$\varphi_{i+1/2} = \begin{cases} \frac{\Delta x_i + \Delta x_{i+1}}{2\Delta x_i} \phi_i(\theta_i) & c > 0 \\ \frac{\Delta x_{i+1} + \Delta x_{i+2}}{2\Delta x_{i+1}} \phi_{i+1}(\theta_{i+1}) & c < 0 \end{cases} \quad (3.20)$$

On the uniform meshes, the equation above confirms that the slope limiters and flux limiters are equivalent to each other. This equivalence is, however, not true on non-uniform meshes. Given linear data, one has from Eq. (2.11)

$$\theta_i = \frac{u_i - u_{i-1}}{u_{i+1} - u_i} = \frac{\Delta x_{i-1} + \Delta x_i}{\Delta x_i + \Delta x_{i+1}}$$

Hence a sufficient condition for second-order space accuracy is $\varphi_{i+1/2} = 1$ or

$$\phi_i \left(\frac{\Delta x_{i-1} + \Delta x_i}{\Delta x_i + \Delta x_{i+1}} \right) = \frac{2\Delta x_i}{\Delta x_i + \Delta x_{i+1}}, \quad \forall i \quad (3.21)$$

Thus in appearance of non-uniform grids, limiter function $\phi_i(\cdot)$ must be defined locally, such that local grid geometry is taken into account.

Finally, the TVD stability condition given by Eqs. (3.11) and the order condition given by Eq. (3.21) are always compatible with each other as shown below

$$0 < \frac{2\Delta x_i}{\Delta x_i + \Delta x_{i+1}} < \frac{2\Delta x_i + 2\Delta x_{i+1}}{\Delta x_i + \Delta x_{i+1}} = 2$$

and

$$0 \cdot \frac{\Delta x_{i-1} + \Delta x_i}{\Delta x_i + \Delta x_{i+1}} < \frac{2\Delta x_i}{\Delta x_i + \Delta x_{i+1}} < 2 \cdot \frac{\Delta x_{i-1} + \Delta x_i}{\Delta x_i + \Delta x_{i+1}}$$

3.3. Revisiting Sweby's diagram. The Sweby's diagram for limiter functions [18] are revisited here to include non-uniform grids. The limiter functions considered satisfy both the TVD stability condition (3.11) and the order condition (3.21).

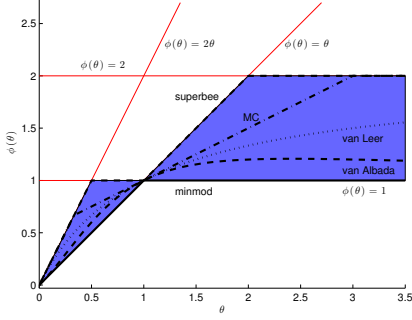
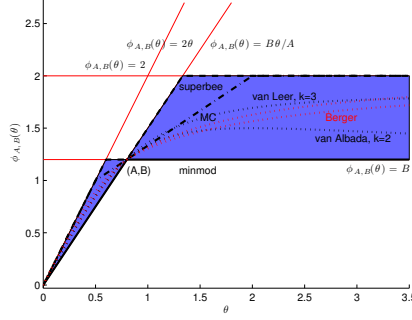
For simplicity, it is assumed that the limiter function $\phi_{A,B}(\cdot)$ is characterized by two parameters A and B which satisfy

$$0 < B < \min(2, 2A) \quad (3.22)$$

and

$$\phi_{A,B}(A) = B \quad (3.23)$$

This notation is used extensively in the remaining of the paper to indicate the enhanced limiter functions that take into account of non-uniform grids. With these notations the conventional limiters are written as $\phi(\cdot) = \phi_{1,1}(\cdot)$, and the corresponding Sweby's diagram is shown in the Figure 3.5. In this diagram, the admissible region of the limiter function is indicated by the shaded region, which is bounded by four straight edges: (1) $\phi(\theta) = 2$, (2) $\phi(\theta) = 2\theta$, (3) $\phi(\theta) = 1$ and (4) $\phi(\theta) = \theta$. The first two edges correspond to the conventional TVD stability conditions given by Eqs. (2.13); and the other two edges are obtained from the Lax-Wendroff method

FIG. 3.5. Sweby's diagram for conventional limiter function $\phi(\cdot) = \phi_{1,1}(\cdot)$ FIG. 3.6. Sweby's diagram for enhanced limiter function $\phi_{A,B}(\cdot)$

[11] as indicated by Eqs. (3.24) and the Beam-Warming method [25] as indicated by Eqs. (3.25) in the case of uniform meshes in space.

$$F_{i+1/2}^{LW,n} = \begin{cases} cu_i^n + \frac{1}{2}c(1-\lambda)(u_{i+1}^n - u_i^n) & c > 0 \\ cu_{i+1}^n - \frac{1}{2}c(1-\lambda)(u_{i+1}^n - u_i^n) & c < 0 \end{cases} \quad (3.24)$$

$$F_{i+1/2}^{BW,n} = \begin{cases} cu_i^n + \frac{1}{2}c(1-\lambda)(u_i^n - u_{i-1}^n) & c > 0 \\ cu_{i+1}^n - \frac{1}{2}c(1-\lambda)(u_{i+2}^n - u_{i+1}^n) & c < 0 \end{cases} \quad (3.25)$$

where $\lambda = |c\Delta t^n|/\Delta x$ is the Courant number on the uniform mesh with cell size Δx . In the view of Eq. (3.12) and Eq. (3.8), the two methods given by Eqs. (3.24)–(3.25) are equivalent to applying the following “slope limiters”

$$\phi^{LW}(\theta) = \begin{cases} 1 & c > 0 \\ \theta & c < 0 \end{cases} \quad (3.26)$$

$$\phi^{BW}(\theta) = \begin{cases} \theta & c > 0 \\ 1 & c < 0 \end{cases} \quad (3.27)$$

Thus the admissible region in the conventional Sweby's diagram is explained such that the limiter function should be a convex combination of ϕ^{LW} and ϕ^{BW} , in addition to satisfying Eqs. (2.13) and Eq. (2.16).

Sweby's diagram is generalized to the limiter function $\phi_{A,B}$ as follows. First, the limiter function ϕ^{LW} and ϕ^{BW} are generalized to satisfy Eq. (3.23) as

$$\phi_{A,B}^{LW}(\theta) = \begin{cases} B & c > 0 \\ \frac{B\theta}{A} & c < 0 \end{cases}, \quad \phi_{A,B}^{BW}(\theta) = \begin{cases} \frac{B\theta}{A} & c > 0 \\ B & c < 0 \end{cases}$$

And the four edges surrounding the admissible region are: (1) $\phi_{A,B}(\theta) = 2$, (2) $\phi_{A,B}(\theta) = 2\theta$, (3) $\phi_{A,B}(\theta) = B$ and (4) $\phi_{A,B}(\theta) = B\theta/A$; and the corresponding Sweby's diagram with the shaded admissible region is illustrated in Figure 3.6.

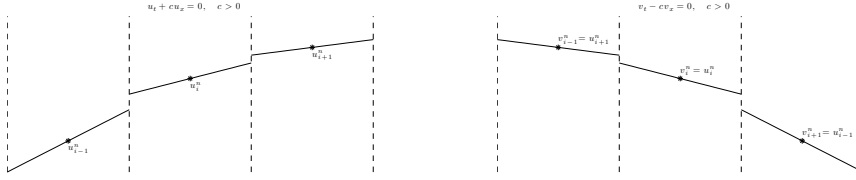


FIG. 3.7. Illustration of symmetry-preserving property on uniform meshes: problem 1 (left); problem 2 (right)

Remark: introducing the two parameters A and B that satisfy Eq. (3.22), one talks about a class of limiter functions rather than a single one when the name of the limiter function is referred to. For example, the enhanced *minmod* limiter (see Section 4) refers to the class of limiter functions that are generalization to the conventional *minmod* limiter function given by Eq. (2.17a) to satisfy Eq. (3.23). In the remaining of the paper, the limiter function without subscript like ϕ^{minmod} refers to the conventional limiter function; whereas the enhanced version is denoted by $\phi_{A,B}^{minmod}$, i.e. a class of limiter functions parameterized by A and B .

3.4. Preserving symmetric solutions. In addition to the TVD stability and formal second-order spatial accuracy properties, the slope limiters are also expected to preserve the symmetric solutions. On uniform meshes, the condition is given by

$$\frac{\phi(\theta)}{\theta} = \frac{1}{\theta} \quad (3.28)$$

It is easy to verify that all the limiters listed in Eqs. (2.17) satisfy this condition.

A geometric interpretation of the symmetry-preserving property of the conventional limiter function $\phi(\cdot)$ is the following. Consider the REP procedure applied with the same uniform mesh to solve two advection problems from time-instance t^n to t^{n+1} for the approximated data in a particular cell Ω_i

1. Problem 1: the governing equation is

$$u_t + cu_x = 0$$

Given data at t^n : u_{i+k}^n , $k = 0, \pm 1, \dots$, use limiter function $\phi(\cdot)$ to solve for the data in Ω_i at the next time-instance t^{n+1} , i.e. u_i^{n+1} .

2. Problem 2: the governing equation is

$$v_t - cv_x = 0$$

Given data at t^n : v_{i+k}^n , $k = 0, \pm 1, \dots$ such that $v_{i+k}^n = u_{i-k}^n$, use the same $\phi(\cdot)$ to solve for the data in Ω_i at the next time-instance t^{n+1} , i.e. v_i^{n+1} .

Then symmetry-preserving is equivalent to $u_i^{n+1} = v_i^{n+1}$. This definition is illustrated in Figure 3.7 in the case $c > 0$, in which the nodes represent the cell-averaged values at time-instance t^n and the slopes represent the reconstructed data after applying the limited slopes (c.f. Figure 3.2).

However, one cannot use the same argument to define the symmetry-preserving property when non-uniform grid is concerned, because the mesh is in general non-symmetric. To this effect, a definition of symmetry-preserving property for a class of slope limiters $\phi_{A,B}(\cdot)$ parameterized by A and B is proposed as follows

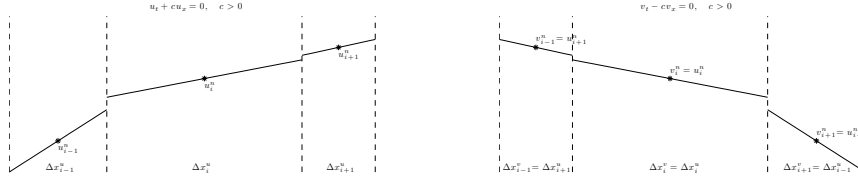


FIG. 3.8. Illustration of symmetry-preserving property on non-uniform meshes: problem 1 (left); problem 2 (right)

DEFINITION 3.2 (Symmetry-preserving). A class of enhanced limiter functions $\phi_{A,B}(\cdot)$ is said to be symmetry-preserving, if the following two problems give rise to

$$u_i^{n+1} = v_i^{n+1}$$

1. Problem 1: the governing equation is

$$u_t + cu_x = 0$$

Given the grid with cell sizes Δx_{i+k}^u and corresponding data at t^n : u_{i+k}^n , $k = 0, \pm 1, \dots$, solve for u_i^{n+1} using the limiter functions $\phi_{A,B}(\cdot)$ satisfying

$$\phi_j^u(\cdot) = \phi_{A_j^u, B_j^u}(\cdot)$$

where $A_j^u = \frac{\Delta x_{j-1}^u + \Delta x_j^u}{\Delta x_j^u + \Delta x_{j+1}^u}$ and $B_j^u = \frac{2\Delta x_j^u}{\Delta x_j^u + \Delta x_{j+1}^u}$, $j = i, i \pm 1, \dots$

2. Problem 2: the governing equation is

$$v_t - cv_x = 0$$

Given the grid with cell sizes Δx_{i+k}^v and corresponding data at t^n : v_{i+k}^n , $k = 0, \pm 1, \dots$, such that $\Delta x_{i+k}^v = \Delta x_{i-k}^u$ and $v_{i+k}^n = u_{i-k}^n$, solve for v_i^{n+1} using the limiter functions $\phi_{A,B}(\cdot)$ satisfying

$$\phi_j^v(\cdot) = \phi_{A_j^v, B_j^v}(\cdot)$$

where $A_j^v = \frac{\Delta x_{j-1}^v + \Delta x_j^v}{\Delta x_j^v + \Delta x_{j+1}^v}$ and $B_j^v = \frac{2\Delta x_j^v}{\Delta x_j^v + \Delta x_{j+1}^v}$, $j = i, i \pm 1, \dots$

Here the superscripts u or v designate one of the two problems to which a particular quantity is relevant. This definition is illustrated in the case $c > 0$, in analogy of Figure 3.7 for uniform meshes, by Figure 3.8. Let $c > 0$, using Eqs. (3.7) and Eq. (3.8), $u_i^{n+1} = v_i^{n+1}$ is equivalent to

$$\begin{aligned} & u_i^n - \lambda_i^u (u_i^n - u_{i-1}^n) - \\ & \frac{1}{2} \lambda_i^u [(1 - \lambda_i^u) \phi_i^u(\theta_i^u)(u_{i+1}^n - u_i^n) - (1 - \lambda_{i-1}^u) \phi_{i-1}^u(\theta_{i-1}^u)(u_i^n - u_{i-1}^n)] \\ & = v_i^n - \lambda_i^v (v_i^n - v_{i+1}^n) + \\ & \frac{1}{2} \lambda_i^v [(1 - \lambda_i^v) \phi_i^v(\theta_i^v)(v_{i+1}^n - v_i^n) - (1 - \lambda_{i+1}^v) \phi_{i+1}^v(\theta_{i+1}^v)(v_{i+2}^n - v_{i+1}^n)] \end{aligned}$$

Employing $v_{i+k}^n = u_{i-k}^n$ and $\Delta x_{i+k}^v = \Delta x_{i-k}^v$ for $k = 0, \pm 1, \dots$

$$\begin{aligned}\lambda_{i+k}^v &= \frac{|c\Delta t^n|}{\Delta x_{i+k}^v} = \frac{|c\Delta t^n|}{\Delta x_{i-k}^u} = \lambda_{i-k}^u \\ \theta_{i+k}^v &= \frac{v_{i+k}^n - v_{i+k-1}^n}{v_{i+k+1}^n - v_{i+k}^n} = \frac{u_{i-k}^n - u_{i-k+1}^n}{u_{i-k-1}^n - u_{i-k}^n} = \frac{1}{\theta_{i-k}^u} \\ A_{i+k}^v &= \frac{\Delta x_{i+k-1}^v + \Delta x_{i+k}^v}{\Delta x_{i+k}^v + \Delta x_{i+k+1}^v} = \frac{\Delta x_{i-k+1}^u + \Delta x_{i-k}^u}{\Delta x_{i-k}^u + \Delta x_{i-k-1}^u} = \frac{1}{A_{i-k}^u} \\ B_{i+k}^v &= \frac{2\Delta x_{i+k}^v}{\Delta x_{i+k}^v + \Delta x_{i+k+1}^v} = \frac{2\Delta x_{i-k}^u}{\Delta x_{i-k}^u + \Delta x_{i-k-1}^u} = \frac{B_{i-k}^u}{A_{i-k}^u}\end{aligned}$$

It follows that

$$\begin{aligned}& u_i^n - \lambda_i^u(u_i^n - u_{i-1}^n) - \\& \frac{1}{2}\lambda_i^u [(1 - \lambda_i^u)\phi_i^u(\theta_i^u)(u_{i+1}^n - u_i^n) - (1 - \lambda_{i-1}^u)\phi_{i-1}^u(\theta_{i-1}^u)(u_i^n - u_{i-1}^n)] \\& = u_i^n - \lambda_i^u(u_i^n - u_{i-1}^n) + \\& \frac{1}{2}\lambda_i^u \left[(1 - \lambda_i^u)\phi_i^v\left(\frac{1}{\theta_i^u}\right)(u_{i-1}^n - u_i^n) - (1 - \lambda_{i-1}^u)\phi_{i-1}^v\left(\frac{1}{\theta_{i-1}^u}\right)(u_{i-2}^n - u_{i-1}^n) \right] \\& = u_i^n - \lambda_i^u(u_i^n - u_{i-1}^n) - \\& \frac{1}{2}\lambda_i^u \left[(1 - \lambda_i^u)\phi_i^v\left(\frac{1}{\theta_i^u}\right)\theta_i^u(u_{i+1}^n - u_i^n) - (1 - \lambda_{i-1}^u)\phi_{i-1}^v\left(\frac{1}{\theta_{i-1}^u}\right)\theta_{i-1}^u(u_i^n - u_{i-1}^n) \right] \\& \tag{3.29}\end{aligned}$$

In the second equality the definition (2.11) is invoked. A sufficient condition for Eq. (3.29) to hold is the following

$$\frac{\phi_{i-k}^u(\theta)}{\theta} = \phi_{i+k}^v\left(\frac{1}{\theta}\right), k = 0, 1$$

Expressing the limiter functions in the form $\phi_{A,B}$ as given in Definition 3.2, this condition is equivalent to

$$\frac{\phi_{A_{i-k}^u, B_{i-k}^u}(\theta)}{\theta} = \phi_{A_{i+k}^v, B_{i+k}^v}\left(\frac{1}{\theta}\right) = \phi_{1/A_{i-k}^u, B_{i-k}^u/A_{i-k}^u}\left(\frac{1}{\theta}\right) \tag{3.30}$$

which suggests the following definition:

DEFINITION 3.3 (Conjugate limiter function). *Given a class of enhanced limiter functions $\phi_{A,B}$ characterized by the two parameters A, B as before, the conjugate class of limiter functions $\phi_{A,B}^*$ is defined by*

$$\phi_{A,B}^* = \phi_{1/A, B/A} \tag{3.31}$$

ϕ^* is well-defined, since for any A, B that satisfy Eq. (3.22), it is always true that

$$0 < \frac{B}{A} < \frac{\min(2, 2A)}{A} = \min(2, \frac{2}{A})$$

In addition, it is clear that

$$\phi_{1/A, B/A}^* = \phi_{1/(1/A), (B/A)/(1/A)} = \phi_{A,B}$$

thus $\phi_{A,B}^{**} = \phi_{A,B}$ for any pair A and B . In the view of Eq. (3.30), a sufficient condition for the symmetry-preserving property is given by

$$\frac{\phi_{A,B}(\theta)}{\theta} = \phi_{A,B}^* \left(\frac{1}{\theta} \right) \quad (3.32)$$

Finally, in the case of conventional limiter functions $\phi = \phi_{1,1}$, the conjugate limiter function is $\phi^* = \phi_{1,1}^* = \phi_{1,1} = \phi$, thus Eq. (3.32) reproduces Eq. (3.28) in the case of uniform meshes.

Remark: an alternative approach to study the symmetry-preserving property is given by M. Berger [2], where a symmetry variable is defined instead of the classical smoothness monitors.

4. Enhanced limiter functions. The conventional limiter function ϕ^{name} given in Eqs. (2.17) (the superscript *name* stands for *minmod*, *MC*, etc.) is enhanced to a class of limiter functions $\phi_{A,B}^{name}$ so that it falls into the admissible region given by the generalized Sweby's diagram (Figure 3.6). The symmetry-preserving condition (3.32) is verified after the construction.

4.1. Enhanced minmod, superbee and MC limiters. ϕ^{minmod} and $\phi^{superbee}$ represent lower and upper boundaries of the Sweby's diagram (Figure 3.5). Thus direct enhancements are given by

$$\phi_{A,B}^{minmod}(\theta) = \max \left(0, \frac{B}{A} \min(\theta, A) \right) \quad (4.1)$$

$$\phi_{A,B}^{superbee}(\theta) = \max \left(0, \min(2\theta, B), \min \left(\frac{B\theta}{A}, 2 \right) \right) \quad (4.2)$$

They are plotted in the generalized Sweby's diagram in Figure 3.6.

The other limiter, ϕ^{MC} , is generalized as below (see also Figure (3.6))

$$\phi_{A,B}^{MC}(\theta) = \max \left(0, \min \left(2\theta, \frac{B}{A+1}(\theta+1), 2 \right) \right) \quad (4.3)$$

Supposing $\theta \neq 0$, the symmetry-preserving property of the three generalized limiters are easily verified below

$$\begin{aligned} \frac{\phi_{A,B}^{minmod}(\theta)}{\theta} &= \max \left(0, \frac{B}{A} \min \left(1, \frac{A}{\theta} \right) \right) = \max \left(0, \frac{B/A}{1/A} \min \left(\frac{1}{A}, \frac{1}{\theta} \right) \right) \\ &= \phi_{1/A, B/A}^{minmod} \left(\frac{1}{\theta} \right) = \phi_{A,B}^{minmod,*} \left(\frac{1}{\theta} \right) \\ \frac{\phi_{A,B}^{superbee}(\theta)}{\theta} &= \max \left(0, \min \left(2, \frac{B}{\theta} \right), \min \left(\frac{B}{A}, \frac{2}{\theta} \right) \right) \\ &= \max \left(0, \min \left(2, \frac{1}{\theta} \cdot \frac{B/A}{1/A} \right), \min \left(\frac{B}{A}, \frac{2}{\theta} \right) \right) \\ &= \max \left(0, \min \left(\frac{2}{\theta}, \frac{B}{A} \right), \min \left(\frac{1}{\theta} \cdot \frac{B/A}{1/A}, 2 \right) \right) = \phi_{1/A, B/A}^{superbee} \left(\frac{1}{\theta} \right) = \phi_{A,B}^{superbee,*} \left(\frac{1}{\theta} \right) \end{aligned}$$

$$\begin{aligned} \frac{\phi_{A,B}^{MC}(\theta)}{\theta} &= \max \left(0, \min \left(2, \frac{B}{A+1} \left(1 + \frac{1}{\theta} \right), \frac{2}{\theta} \right) \right) \\ &= \max \left(0, \min \left(\frac{2}{\theta}, \frac{B/A}{1/A+1} \left(\frac{1}{\theta} + 1 \right), 2 \right) \right) = \phi_{1/A, B/A}^{MC} \left(\frac{1}{\theta} \right) = \phi_{A,B}^{MC,*} \left(\frac{1}{\theta} \right) \end{aligned}$$

4.2. Enhanced *van Leer* limiter. Two generalized *van Leer* limiters are proposed in [2] in terms of symmetry variables, which can be reformulated in the notations of this paper as the following

$$\phi_{A,B}^{Berger-1}(\theta) = \begin{cases} 2\theta \left[1 - \left(1 - \frac{B}{2A} \right) \left[\frac{\theta}{\theta+1} \cdot \frac{A+1}{A} \right]^{\frac{B}{2A-B}} \right] & \theta \leq A \\ 2 \left[1 - \left(1 - \frac{B}{2} \right) \left[\frac{A+1}{\theta} \right]^{\frac{B}{2-B}} \right] & \theta > A \end{cases} \quad (4.4)$$

$$\phi_{A,B}^{Berger-2}(\theta) = \begin{cases} \frac{B(\theta+1)}{A+1} \left[1 - \left(1 - \frac{\theta}{\theta+1} \cdot \frac{A+1}{A} \right)^{\frac{2A}{B}} \right] & \theta \leq A \\ \frac{B(\theta+1)}{A+1} \left[1 - \left(1 - \frac{A+1}{\theta+1} \right)^{\frac{2}{B}} \right] & \theta > A \end{cases} \quad (4.5)$$

Both limiters reduce to the conventional *van Leer* limiter given by Eq. (2.17d) in the case $A = B = 1$; and both satisfy the TVD stability condition, order condition and symmetry-preserving condition. They are plotted in Figure 3.6.

A drawback of these two modifications is that they are not smooth at the point $\theta = A$, whereas the conventional $\phi_{A,B}^{van\ Leer}$ is smooth for all $\theta > 0$. A smooth enhancement, denoted by $\phi_{A,B}^{van\ Leer}$ is provided here.

Noticing that

$$\lim_{k \rightarrow \infty} \frac{A^k + A^{k-1} + \dots + A}{A^k + A^{k-1} + \dots + A + 1} = \min(1, A)$$

and in the view of Eq. (3.22), there always exists an integer k , such that

$$B \leq \frac{2(A^k + A^{k-1} + \dots + A)}{A^k + A^{k-1} + \dots + A + 1} \quad (4.6)$$

The enhanced *van Leer* limiter is defined as

$$\phi_{A,B}^{van\ Leer}(\theta) = \begin{cases} \frac{B(\theta^k + \theta^{k-1} + \dots + \theta)}{\theta^k + \theta^{k-1} + \dots + \theta + 1} \cdot \frac{A^k + A^{k-1} + \dots + A + 1}{A^k + A^{k-1} + \dots + A} & \theta \geq 0 \\ 0 & \theta < 0 \end{cases} \quad (4.7)$$

To verify the TVD stability condition, supposing $\theta \geq 0$, it is sufficient to apply Eq. (4.6) to show that

$$\phi_{A,B}^{van\ Leer} \leq \frac{2(\theta^k + \theta^{k-1} + \dots + \theta)}{\theta^k + \theta^{k-1} + \dots + \theta + 1} < 2 \min(1, \theta)$$

The order condition given by Eq. (3.23) is verified by the following equality

$$\phi_{A,B}^{van\ Leer}(A) = \frac{B(A^k + A^{k-1} + \dots + A)}{A^k + A^{k-1} + \dots + A + 1} \cdot \frac{A^k + A^{k-1} + \dots + A + 1}{A^k + A^{k-1} + \dots + A} = B$$

Finally, the symmetry-preserving condition is verified as following

$$\begin{aligned}
\frac{\phi_{A,B}^{van\ Leer}(\theta)}{\theta} &= \frac{B(\theta^{k-1} + \theta^{k-2} + \dots + \theta + 1)}{\theta^k + \theta^{k-1} + \dots + \theta + 1} \cdot \frac{A^k + A^{k-1} + \dots + A + 1}{A^k + A^{k-1} + \dots + A} \\
&= \frac{(B/A) \cdot A \cdot \theta^k(\theta^{-1} + \theta^{-2} + \dots + \theta^{1-k} + \theta^{-k})}{\theta^k(1 + \theta^{-1} + \dots + \theta^{-k})} \cdot \frac{A^k(1 + A^{-1} + \dots + A^{-k})}{A^{k+1}(A^{-1} + A^{-2} + \dots + A^{-k})} \\
&= \frac{(B/A)(\theta^{-1} + \theta^{-2} + \dots + \theta^{1-k} + \theta^{-k})}{1 + \theta^{-1} + \dots + \theta^{-k}} \cdot \frac{1 + A^{-1} + \dots + A^{-k}}{A^{-1} + A^{-2} + \dots + A^{-k}} \\
&= \phi_{1/A, B/A}^{van\ Leer}\left(\frac{1}{\theta}\right) = \phi_{A,B}^{van\ Leer,*}\left(\frac{1}{\theta}\right)
\end{aligned}$$

A sample curve calculated with $k = 3$ is plotted in Figure 3.6. And clearly, if $A = B = 1$, Eq. (4.6) is satisfied by $k = 1$, in which case the enhanced limiter Eq. (4.7) reduces to the conventional *van Leer* limiter.

Remark: This particular limiter can be used as a good example to show that, the issue raised in this paper cannot always be resolved by choosing a different smoothness monitor and at the same time applying the conventional limiter function. See the proof in Appendix B.

4.3. Enhanced van Albada limiter. The *van Albada* limiter $\phi^{van\ Albada}$ is sometimes preferred over $\phi^{van\ Leer}$ since the former is less restrictive in certain regions of θ . The enhanced *van Albada* limiter proposed here remains a smooth function of the smoothness monitor, and is based on the following inequality

$$\lim_{k \rightarrow \infty} \frac{(k-1)^{k-1}}{k^k} = 0$$

so that given A and B satisfying Eq. (3.22), there always exists k such that

$$B \leq 2 \left(1 + \frac{(k-1)^{k-1}}{k^k} \right)^{-1} \min(A, 1) \quad (4.8)$$

Then the limiter function is defined as

$$\phi_{A,B}^{van\ Albada}(\theta) = \frac{B(\theta^k + \theta)}{\theta^k + A} \quad (4.9)$$

To verify the TVD stability condition, one need to show $\phi_{A,B}^{van\ Albada}(\theta) \leq 2 \min(1, \theta)$ for all $\theta > 0$, as the following

$$\frac{B(\theta^k + \theta)}{\theta^k + A} \leq 2 \Leftrightarrow \left(\frac{2}{B} - 1 \right) \theta^k + \frac{2A}{B} \geq \theta \Leftrightarrow \left(\frac{2}{B} - 1 \right) \theta^k + (k-1) \cdot \frac{2A}{(k-1)B} \geq \theta$$

The last inequality always holds due to the inequality of geometric and arithmetic means

$$\left(\frac{2}{B} - 1 \right) \theta^k + (k-1) \cdot \frac{2A}{(k-1)B} \geq k \left(\frac{2}{B} - 1 \right)^{\frac{1}{k}} \left(\frac{2A}{k-1} \right)^{\frac{k-1}{k}} \theta \geq \theta$$

where the last inequality holds because of Eq. (4.8).

In addition

$$\frac{B(\theta^k + \theta)}{\theta^k + A} \leq 2\theta \Leftrightarrow \left(\frac{2A}{B} - 1 \right) \frac{1}{\theta^k} + \frac{2}{B} \geq \frac{1}{\theta} \Leftrightarrow \left(\frac{2A}{B} - 1 \right) \frac{1}{\theta^k} + (k-1) \cdot \frac{2}{(k-1)B} \geq \frac{1}{\theta}$$

and following the same reasoning one concludes $\phi_{A,B}^{van Albada}(\theta) \leq 2\theta$.

The order condition $\phi_{A,B}^{van Albada}(A) = B$ is clearly satisfied according to Eq. (4.9); and the symmetry-preserving condition is shown as follows

$$\begin{aligned} \frac{\phi_{A,B}^{van Albada}(\theta)}{\theta} &= \frac{B(\theta^{k-1} + 1)}{\theta^k + A} = \frac{(B/A)\theta^k(\theta^{-1} + \theta^{-k})}{\theta^k(1/A + \theta^{-k})} = \frac{(B/A)(\theta^{-k} + \theta^{-1})}{\theta^{-k} + 1/A} \\ &= \phi_{1/A, B/A}^{van Albada}\left(\frac{1}{\theta}\right) = \phi_{A,B}^{van Albada,*}\left(\frac{1}{\theta}\right) \end{aligned}$$

An example curve with $k = 2$ is provided in Figure 3.6. In addition, when $k = 1$, the enhanced limiter Eq. (4.9) coincides with the conventional one given also that $A = B = 1$.

Remark: in practice, evaluating the right hand side of Eq. (4.8) can be expensive, and an economical alternative is due to the observation that

$$\frac{(k-1)^{k-1}}{k^k} = \left(\frac{k-1}{k}\right)^{k-1} \cdot \frac{1}{k} \leq \frac{1}{k}, \quad \forall k \geq 1$$

thus in the numerical examples to be presented, the value k is computed such that the following condition is satisfied

$$B \leq 2 \left(1 + \frac{1}{k}\right)^{-1} \min(1, A)$$

5. Numerical examples.

5.1. Convergence tests. For all the numerical examples here to show the convergence behavior when the solutions are known to be smooth, the five enhanced limiters given in previous section as well as the two modified *van Leer* limiters by M. Berger are tested. Two parameters $r = 0.2$ and $r = 0.3$ are used to generate the non-uniform meshes as described in Section 2.

5.1.1. One-dimensional smooth Euler problem. The same problem described in Section 2 is solved here with the enhanced limiter functions. With each value of the parameter r , five meshes with number of cells ranging from 100 to 1600 are generated independently to test the convergence behavior. The L_1 norms of errors in computed pressure are plotted in Figure 5.1 for the parameters $r = 0.2$ and $r = 0.3$. Together with the first-order Godunov scheme where no linear reconstruction is applied (referred to in the figure as $\phi = 0$), the limiter functions chosen to be reflected in the figures are: conventional *minmod* limiter, conventional *van Albada* limiter, enhanced *minmod* limiter, enhanced *van Albada* limiter and the two modified *van Leer* limiters by M. Berger.

Furthermore, all the computed convergence rates are reported in Table 5.1 and Table 5.2 for the parameter $r = 0.2$ and $r = 0.3$ respectively.

The conclusions from the results are

1. On non-uniform meshes, the solutions obtained from applying conventional limiters, though only show first order convergence, are in general more accurate than first-order schemes, as shown in Figure 5.1. MUSCL with the enhanced limiters generally show higher-order convergence rates and smaller errors than the first order scheme and MUSCL with conventional limiter functions.

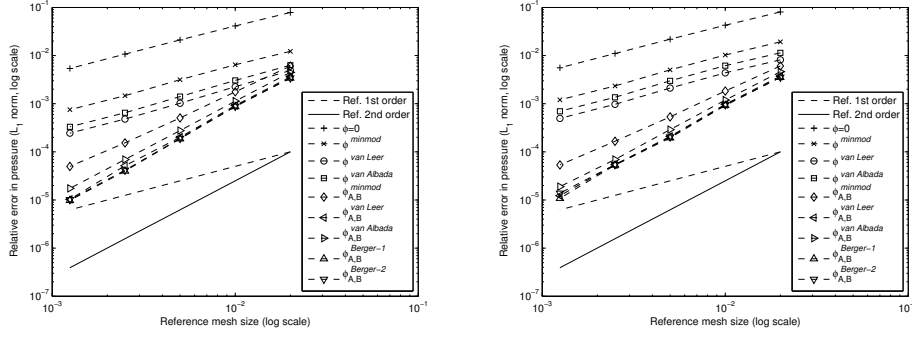


FIG. 5.1. Convergence rates in pressure achieved with selected limiter functions on non-uniform meshes generated by: $r = 0.2$ (left) and $r = 0.3$ (right)

TABLE 5.1

Convergence rates achieved on non-uniform meshes with $r = 0.2$ by applying enhanced limiters

	minmod	superbee	MC	van Leer	van Albada	Berger-1	Berger-2
ρ	1.6603	1.3193	2.0490	2.0935	1.9620	2.0888	2.0742
u	1.7309	1.5222	2.0645	2.1103	2.0645	2.1063	2.0978
p	1.7308	1.4729	2.0566	2.1119	2.0023	2.1088	2.1003

2. Among the enhanced limiters, $\phi_{A,B}^{\minmod}$ and $\phi_{A,B}^{\superbee}$ are less accurate than the others, though convergence rates above first-order are observed.
3. The enhanced limiters $\phi_{A,B}^{MC}$, $\phi_{A,B}^{\van Leer}$, $\phi_{A,B}^{\van Albada}$ together with the two limiters $\phi_{A,B}^{\Berger-1}$, $\phi_{A,B}^{\Berger-2}$ recover second-order convergence in all fluid state variables almost perfectly.

5.1.2. Two-dimensional smooth Euler problem. The two-dimensional test is given by the isentropic vortex advection problem [16]. The governing equation is the 2D Euler equations

$$\mathbf{w}_t + \mathbf{f}(\mathbf{w})_x + \mathbf{g}(\mathbf{w})_y = 0$$

$$\mathbf{w} = \begin{bmatrix} \rho \\ \rho u \\ \rho v \\ E \end{bmatrix}, \quad \mathbf{f}(\mathbf{w}) = \begin{bmatrix} \rho u \\ \rho u^2 + p \\ \rho uv \\ u(E + p) \end{bmatrix}, \quad \mathbf{g}(\mathbf{w}) = \begin{bmatrix} \rho v \\ \rho uv \\ \rho v^2 + p \\ v(E + p) \end{bmatrix} \quad (5.1)$$

where u and v are velocity components in x - and y - directions, and the total energy per unit volume is hence defined as

$$E = \rho e + \frac{1}{2} \rho (u^2 + v^2)$$

The equation of state is the same as that given in Section 2 for 1D Euler equations. The computational domain is $(x, y) \in [-5, 5] \times [-5, 5]$ with periodic boundary condi-

TABLE 5.2

Convergence rates achieved on non-uniform meshes with $r = 0.3$ by applying enhanced limiters

	minmod	superbee	MC	van Leer	van Albada	Berger-1	Berger-2
ρ	1.6331	1.3647	2.0566	2.0118	1.9770	2.0603	1.8940
u	1.7026	1.5312	2.0708	2.0834	2.0496	2.0931	2.0534
p	1.7069	1.5222	2.0646	2.0620	1.9821	2.0865	1.9080

tions. The initial condition is given by

$$\begin{aligned}
u(x, y, 0) &= 1 - \frac{\epsilon y}{2\pi} \exp\left(\frac{1}{2}(1 - x^2 - y^2)\right) \\
v(x, y, 0) &= 1 + \frac{\epsilon x}{2\pi} \exp\left(\frac{1}{2}(1 - x^2 - y^2)\right) \\
\rho(x, y, 0) &= \left(1 - \frac{(\gamma - 1)\epsilon^2}{8\gamma\pi^2} \exp(1 - x^2 - y^2)\right)^{\frac{1}{\gamma-1}} \\
p(x, y, 0) &= \left(1 - \frac{(\gamma - 1)\epsilon^2}{8\gamma\pi^2} \exp(1 - x^2 - y^2)\right)^{\frac{\gamma}{\gamma-1}}
\end{aligned}$$

and the parameter ϵ is chosen to be $\epsilon = 5$. The initial condition gives rise to an isentropic vortex with uniform entropy $s = p/\rho^\gamma = 1$; and the vortex's motion is described by advection in the $(1, 1)$ direction. After one period of time $T = 10.0$, the exact solution is the same as the initial condition, which is employed to calculate the errors of the numerical solutions.

The problem is solved numerically on non-uniform Cartesian grids, which are generated in a way such that the non-uniform spacing in x - and y - directions are performed independently according to the algorithm given in Section 2 for the 1D case. When linear reconstruction is applied, MUSCL technique with chosen slope limiters are performed via a dimension-splitting manner. For all the simulations presented, second-order TVD Runge-Kutta time-integrator is employed.

The initial pressure contour is provided in Figure 5.2 together with the solution computed using first order Godunov scheme (Figure 5.3); with a non-uniform grid generated with the parameter $r = 0.2$, the solutions computed using MUSCL with conventional *van Albada* limiter (Figure 5.4) and the enhanced version $\phi_{A,B}^{van Albada}$ (Figure 5.5).

It is evident from the Figures 5.2–5.5 that, MUSCL technique gives much more accurate solutions to the first order scheme; and among the two simulations calculated with MUSCL technique, the one using the enhanced *van Albada* limiter is even more accurate than the one using the conventional *van Albada* limiter.

Similar as in the previous 1D tests, the convergence behavior of L_1 norms of errors in pressure are plotted in Figure 5.6 for selected slope limiters. For all the simulations, four meshes with number of cells ranging from 20×20 to 160×160 are employed for the purpose of evaluating the convergence behavior.

The convergence rates calculated using the two finest meshes are reported in Table 5.3 and Table 5.4 for the parameters $r = 0.2$ and $r = 0.3$ respectively.

The following conclusions can be drawn from the numerical results

1. On non-uniform Cartesian meshes, MUSCL with conventional limiters are

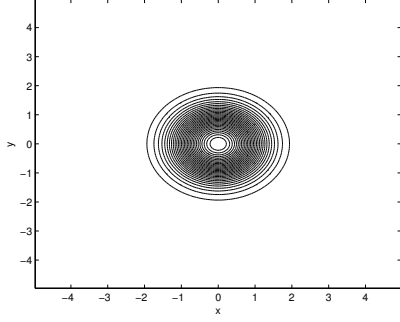


FIG. 5.2. Initial pressure for the isentropic vortex advection problem

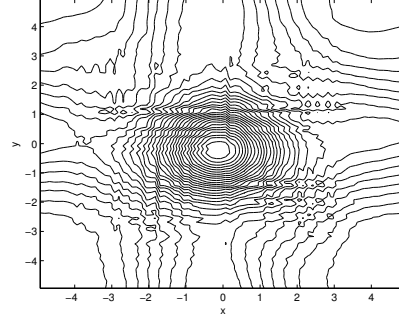


FIG. 5.3. Pressure at $T = 10$ computed by first order Godunov scheme on non-uniform mesh.

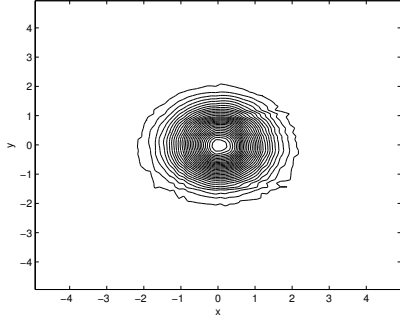


FIG. 5.4. Pressure at $T = 10$ computed by MUSCL with $\phi^{van Albada}$ on non-uniform mesh.

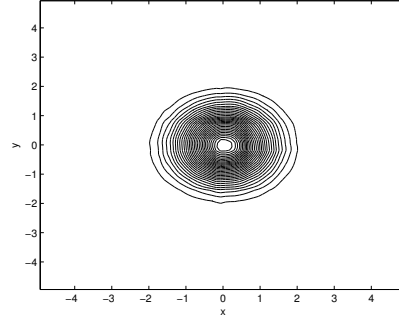


FIG. 5.5. Pressure at $T = 10$ computed by MUSCL with $\phi_{A,B}^{van Albada}$ on non-uniform mesh.

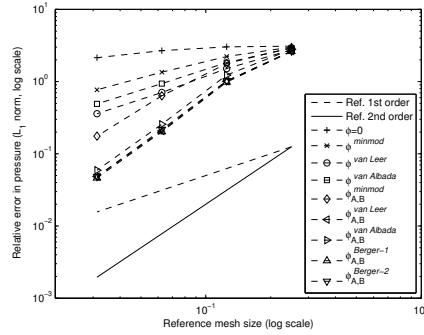
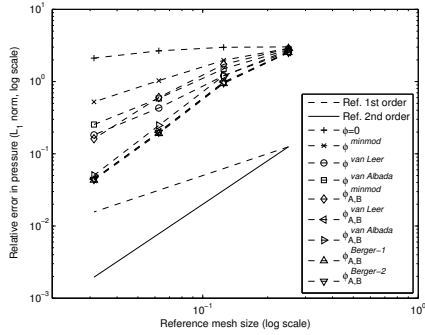


FIG. 5.6. Convergence rates in pressure achieved with selected limiter functions on non-uniform meshes generated by: $r = 0.2$ (left) and $r = 0.3$ (right)

more accurate than first order Godunov scheme, whereas they are less accurate than MUSCL equipped with the enhanced limiters.

2. In terms of convergence rates, when the meshes are sufficiently refined, the formal first-order Godunov scheme presents convergence rate below first-order; the conventional limiters in MUSCL framework give asymptotic first order

TABLE 5.3

Convergence rates achieved on non-uniform meshes with $r = 0.2$ by applying enhanced limiters

	minmod	superbee	MC	van Leer	van Albada	Berger-1	Berger-2
ρ	1.8798	1.5014	1.8667	2.0177	2.1506	2.0093	2.0251
u	1.7014	1.6180	1.9089	1.9058	1.8651	1.9254	1.9165
v	1.6776	1.6496	1.9617	1.9452	1.9058	1.9620	1.9514
p	1.8982	1.5557	1.9255	2.1539	2.2957	2.1474	2.1681

TABLE 5.4

Convergence rates achieved on non-uniform meshes with $r = 0.3$ by applying enhanced limiters

	minmod	superbee	MC	van Leer	van Albada	Berger-1	Berger-2
ρ	1.8339	1.4765	1.8499	1.9765	2.0095	1.9949	2.0254
u	1.6970	1.5680	1.9060	1.8959	1.8178	1.9246	1.9054
v	1.6599	1.6058	1.9610	1.9224	1.8052	1.9523	1.9279
p	1.8549	1.4981	1.9130	2.0986	2.1158	2.1303	2.1654

convergence; and second order convergences is recovered by the enhanced limiters except for $\phi_{A,B}^{minmod}$ and $\phi_{A,B}^{superbee}$, in which case convergence rates between 1.5 and 2.0 are observed.

5.2. Suppression of oscillations near discontinuities. An important purpose of applying limiters is to enhance the stability property of the numerical algorithm, especially near discontinuities. The ability of the enhanced limiters to suppress spurious oscillations on non-uniform grids is illustrated by 1D and 2D benchmark problems in this section. For all the test problems, numerical results calculated with conventional and enhanced *minmod* limiter and *van Albada* limiter are presented; applications with other limiter functions lead to similar conclusions.

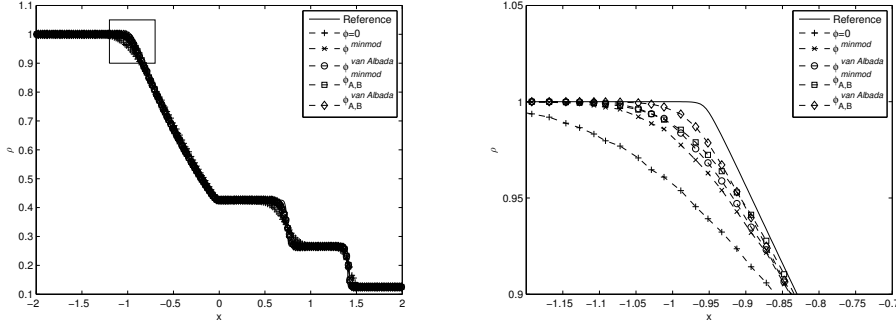
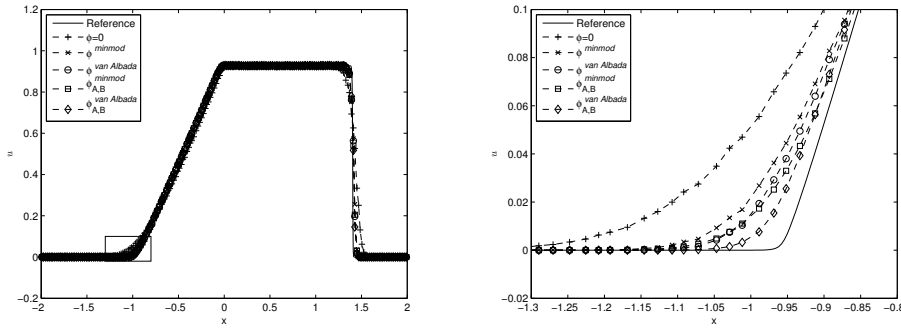
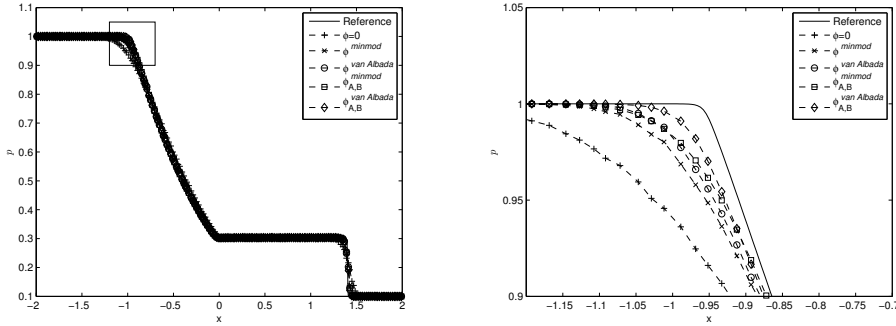
5.2.1. One-dimensional shock tube problem. The first problem is the classical Sod's shock tube problem [17], which is governed by the 1D Euler equations in the domain $x \in [-2, 2]$, with initial condition given in primitive variables as

$$\begin{cases} \rho(x, 0) = 1.0 \\ u(x, 0) = 0.0 \\ p(x, 0) = 1.0 \end{cases} \quad x < 0 \quad \begin{cases} \rho(x, 0) = 0.125 \\ u(x, 0) = 0.0 \\ p(x, 0) = 0.1 \end{cases} \quad x > 0 \quad (5.2)$$

The problem is solved to $T = 0.8$. The solution is composed of a left-going rarefaction, a right-going contact discontinuity and a right-going shock. The density, velocity and pressure profiles at terminal time are plotted in the left columns of Figures 5.7–5.9; and the enlarged local views are provided in the right columns. All the simulations are computed with 200 cells in space and irregularity parameter $r = 0.3$; the CFL number calculated with the reference cell size is chosen to be 0.6. It is clear that the three non-linear waves are all resolved well for all the schemes tested.

It is clear from the figures

1. The MUSCL schemes (with conventional limiters or enhanced limiters) are more accurate than the first order Godunov scheme (that corresponds to the case $\phi = 0$ in the figures).
2. No spurious oscillations is visually observable for all the MUSCL schemes, either with conventional limiters or with enhanced limiters. This falls in line

FIG. 5.7. Density at $T = 0.8$: global profile (left) and local profile (right)FIG. 5.8. Velocity at $T = 0.8$: global profile (left) and local profile (right)FIG. 5.9. Velocity at $T = 0.8$: global profile (left) and local profile (right)

with the previous arguments that the TVD stability conditions are the same for both uniform and non-uniform meshes.

3. The enhanced limiters provide more accurate solutions than the conventional limiters, which is evident by comparing solution curves computed with ϕ^{minmod} and $\phi_{A,B}^{minmod}$, or those computed with $\phi^{van Albada}$ and $\phi_{A,B}^{van Albada}$.

The second example is the double-shock problem [12] which is governed by 1D Euler

equations on the domain $x \in [-3, 3]$ with initial condition given in primitive variables

$$\begin{cases} \rho(x, 0) = 1.0 \\ u(x, 0) = 3.0 \\ p(x, 0) = 1.0 \end{cases} \quad x < 0 \quad \begin{cases} \rho(x, 0) = 2.0 \\ u(x, 0) = 1.0 \\ p(x, 0) = 1.0 \end{cases} \quad x > 0 \quad (5.3)$$

The terminal time of simulation is chosen to be $T = 0.8$. The solution is composed of a slow right-going shock wave, a right-going contact discontinuity and a fast right-going shock wave. This is a more challenging problem than the previous one, mainly due to the fact that the density peak between the contact discontinuity and the fast shock wave is difficult to capture. 150 cells generated with parameter $r = 0.3$ are employed for all the simulations, and CFL number computed with the reference cell size is chosen to be 0.6. The density, velocity and pressure profiles are given in Figures 5.10–5.12, with the left columns being global view and the right columns being local details.

From the figures one can conclude

1. The MUSCL schemes (with conventional limiters or enhanced limiters) are more accurate than the first order Godunov scheme, especially in resolving the density peak near $x = 1.7$ as shown in the right part of Figure 5.10.
2. A few oscillations are observed for pressure between the two shocks, whichever limiter function (conventional or enhanced) is applied with MUSCL. This violation of the TVD stability can be largely explained by the nonlinearity of the Euler equations, and the point here is that both conventional and enhanced limiters present similar stability behaviors.
3. The enhanced limiters lead to more accurate solution in density than the conventional counterparts do; whereas the difference in velocity and pressure are less distinguishable.

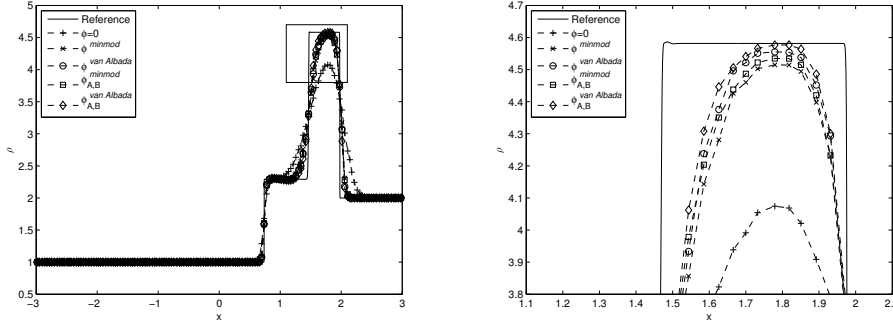
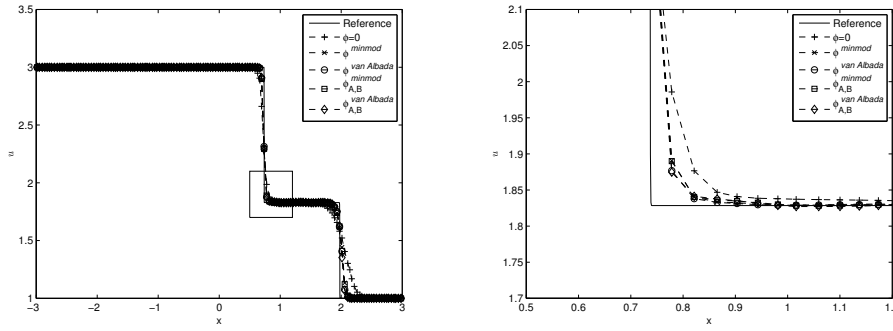
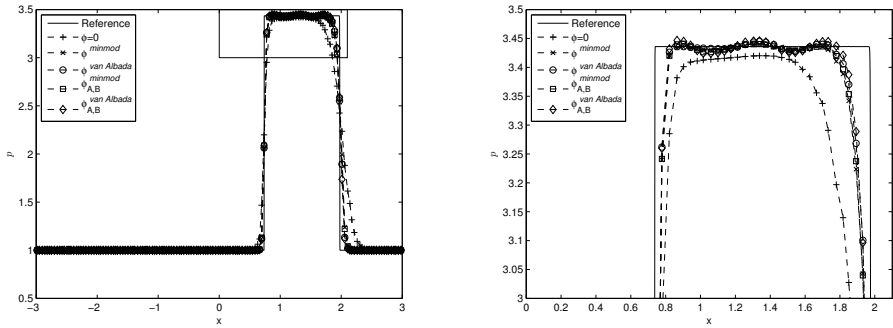
The last 1D example in this section is the Woodward-Colella blast-wave problem [26], governed by 1D Euler equations on the domain $x \in [0, 1]$ with piecewise constant initial conditions given in primitive variables

$$\begin{cases} \rho(x, 0) = 1.0 \\ u(x, 0) = 0.0 \\ p(x, 0) = 1000.0 \end{cases} \quad 0 < x < 0.1 \quad \begin{cases} \rho(x, 0) = 1.0 \\ u(x, 0) = 0.0 \\ p(x, 0) = 0.01 \end{cases} \quad 0.1 < x < 0.9 \\ \begin{cases} \rho(x, 0) = 1.0 \\ u(x, 0) = 0.0 \\ p(x, 0) = 100.0 \end{cases} \quad 0.9 < x < 1 \end{cases} \quad (5.4)$$

The two boundary conditions are given by reflective walls. The problem is solved up to $T = 0.038$. This problem is characterized by large pressure ratios in the initial condition, and a collision of shock waves at around $t = 0.027$; and the final solution presents both large ratios in density and in pressure. Numerical results are computed with 200 non-uniform cells generated with $r = 0.3$, and CFL number calculated with reference cell-size fixed to be 0.6. The solution curves are provided in Figures 5.13–5.15.

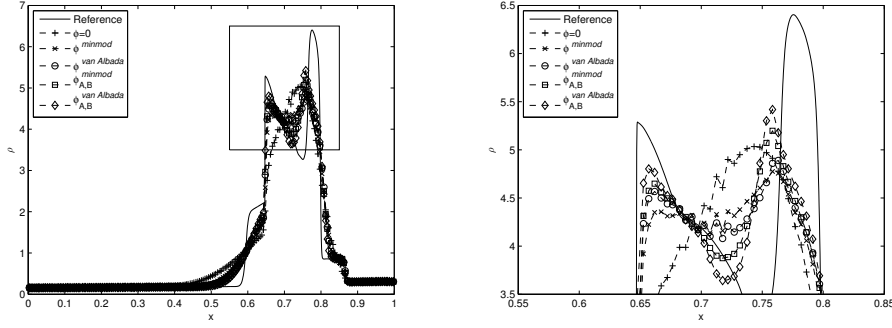
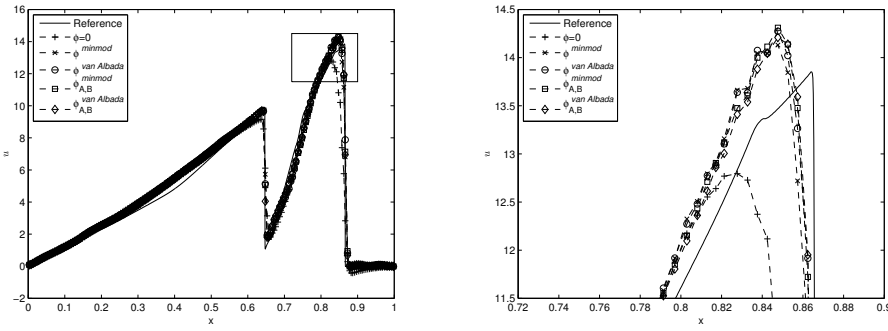
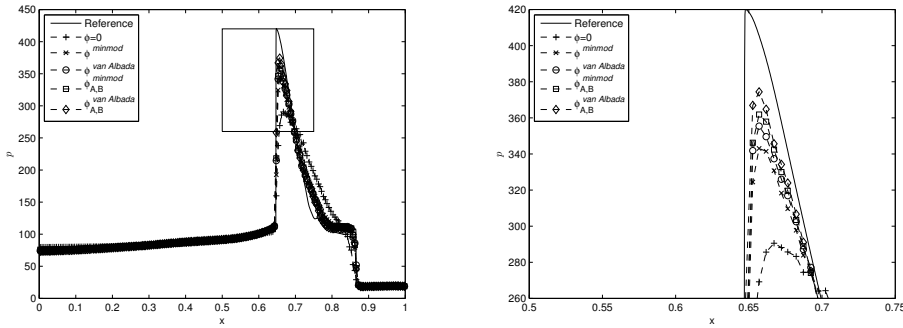
From the figures one observes

1. The first-order scheme gives totally wrong solution between the two density peaks near $x = 0.65$ and $x = 0.8$, due to the excessive numerical dissipation; MUSCL with conventional limiters lead to roughly correct solution in this region, but with small oscillations; and the enhanced limiters compute the correct shape, and oscillation-free solutions. In addition, between the two enhanced limiters shown, $\phi_{A,B}^{van\ Albada}$ leads to more accurate than $\phi_{A,B}^{minmod}$.

FIG. 5.10. Density at $T = 0.8$: global profile (left) and local profile (right)FIG. 5.11. Velocity at $T = 0.8$: global profile (left) and local profile (right)FIG. 5.12. Velocity at $T = 0.8$: global profile (left) and local profile (right)

2. All MUSCL schemes tested produce more accurate velocities than the first-order scheme, and these solutions show similar stability property and are hardly distinguishable from each other.
3. Enhanced limiters lead to more accurate pressure at the peak than the conventional ones; whereas they are all much more accurate than the first-order scheme.

5.2.2. Two-dimensional Euler problem. Two two-dimensional problems are tested. Both problems are governed by the 2D Euler equations. The meshes are

FIG. 5.13. *Density at $T = 0.038$: global profile (left) and local profile (right)*FIG. 5.14. *Velocity at $T = 0.038$: global profile (left) and local profile (right)*FIG. 5.15. *Velocity at $T = 0.038$: global profile (left) and local profile (right)*

obtained in the same way as in the previous isentropic vortex advection example. The first problem is a Mach 3 wind tunnel with a step [26], in which the wind tunnel is given by the domain $(x, y) \in [0, 3] \times [0, 1]$, and the step is placed at $x = 0.6$ and with height 0.2, as shown in Figures 5.16–5.18. Wall boundary conditions are specified at upper wall of the wind tunnel, lower wall of the wind tunnel before the step, and the left- and upper-boundaries of the step. Incoming flow condition

$$\rho(0, y, t) = 1.4, \quad u(0, y, t) = 3.0, \quad v(0, y, t) = 0.0, \quad p(0, y, t) = 1.0$$

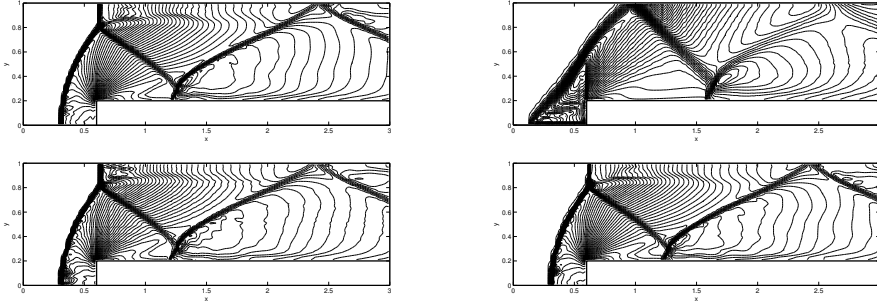


FIG. 5.16. Density at $T = 4.0$ calculated on: uniform mesh with $\phi^{van Albada}$ (upper-left); non-uniform mesh ($r = 0.3$) with first-order Godunov scheme (upper-right); non-uniform mesh ($r = 0.3$) with $\phi^{van Albada}$; non-uniform mesh ($r = 0.3$) with $\phi_{A,B}^{van Albada}$

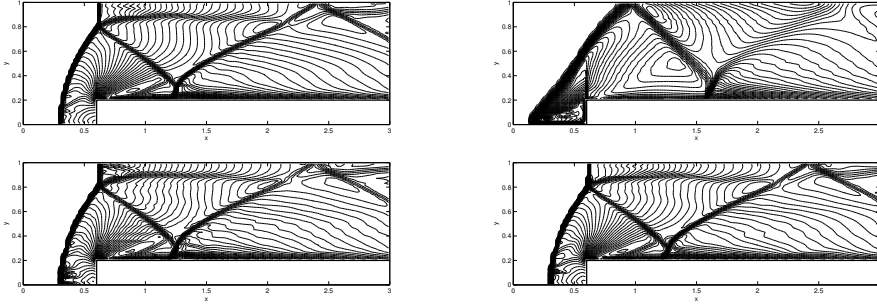


FIG. 5.17. Mach number at $T = 4.0$ calculated on: uniform mesh with $\phi^{van Albada}$ (upper-left); non-uniform mesh ($r = 0.3$) with first-order Godunov scheme (upper-right); non-uniform mesh ($r = 0.3$) with $\phi^{van Albada}$; non-uniform mesh ($r = 0.3$) with $\phi_{A,B}^{van Albada}$

is specified at the left opening of the wind tunnel; whereas the outgoing flow condition at $x = 3.0$ is given by homogeneous Neumann boundary condition

$$\rho_x(3, y, t) = 0.0, \quad u_x(3, y, t) = 0.0, \quad v_x(3, y, t) = 0.0, \quad p_x(3, y, t) = 0.0$$

At the terminal time $T = 4.0$, the solution presents shock-shock interactions, shock-boundary layer interactions and shock-wall reflections, where the boundary layer is generated at the corner of the step which is a singular point in the flow. Numerical solutions computed on both uniform and non-uniform (with $r = 0.3$) 150×50 (which number includes those immersed in the step) meshes are presented as 50 contours for density, Mach number and pressure in Figure 5.16, Figure 5.17 and Figure 5.18 respectively. Among the four simulations, MUSCL with $\phi^{van Albada}$ is applied for the uniform mesh, and the results are reported in the upper-left parts of the figures. For the non-uniform meshes, results computed from first order Godunov scheme are presented in the upper-right parts of the figures; MUSCL with conventional limiter $\phi^{van Albada}$ in the lower-left parts, and MUSCL with enhanced limiter $\phi_{A,B}^{van Albada}$ are in the lower-right parts.

From the figures one conclude

1. All the simulations lead to stable results.
2. The first order scheme produce wrong results, since the interaction between the first shock wave and the reflected shock wave from upper wall is not

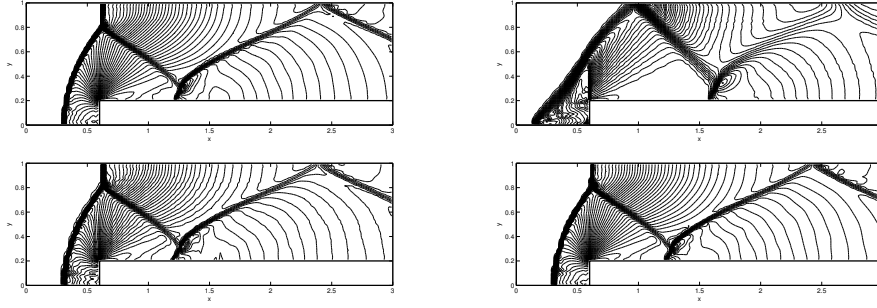


FIG. 5.18. Pressure at $T = 4.0$ calculated on: uniform mesh with $\phi^{van\ Albada}$ (upper-left); non-uniform mesh ($r = 0.3$) with first-order Godunov scheme (upper-right); non-uniform mesh ($r = 0.3$) with $\phi^{van\ Albada}$; non-uniform mesh ($r = 0.3$) with $\phi_{A,B}^{van\ Albada}$

captured at all.

3. Using the numerical results computed on the uniform mesh (upper-left parts) as reference, MUSCL with enhanced limiter $\phi_{A,B}^{van\ Albada}$ leads to almost identical contours; whereas MUSCL with conventional limiter $\phi^{van\ Albada}$ gives rise to less accurate solutions, especially in the following regions: 1. After the shock front on the lower wall in front of the step (near the location $(0.3, 0.0)$ on the lower wall); 2. After the first reflected shock from upper wall (near the location $(0.6, 1.0)$ on the upper wall).

The second problem is the double Mach reflection of a Mach 10 shock [26]. The physical setup for the problem can be found in the paper cited; the numerical problem setup is given below. The computational domain is $(x, y) \in [0, 4] \times [0, 1]$, which is discretized by uniform or non-uniform Cartesian meshes. The initial condition is given by flow separated by a Mach 10 shock, located along the straight line $x = 1/6 + y/\sqrt{3}$. The flow state vector to the left of the shock is given by the post-shock status

$$\begin{cases} \rho(x, y, 0) = 8.0 \\ u(x, y, 0) = 8.25 \cos\left(\frac{\pi}{6}\right) \\ v(x, y, 0) = -8.25 \sin\left(\frac{\pi}{6}\right) \\ p(x, y, 0) = 116.5 \end{cases} \quad x < \frac{1}{6} + \frac{y}{\sqrt{3}} \quad (5.5)$$

and the flow state vector to the right of the shock is given by the pre-shock status

$$\begin{cases} \rho(x, y, 0) = 1.4 \\ u(x, y, 0) = 0.0 \\ v(x, y, 0) = 0.0 \\ p(x, y, 0) = 1.0 \end{cases} \quad x > \frac{1}{6} + \frac{y}{\sqrt{3}} \quad (5.6)$$

The in-flow condition at $x = 0$ and flow condition on the lower boundary before $x = 1/6$ are given by the post-shock fluid state vector Eqs. (5.5) for all time; the out-flow boundary condition at $x = 4$ is the homogeneous Neumann boundary condition

$$\rho_x(4, y, t) = 0.0, \quad u_x(4, y, t) = 0.0, \quad v_x(4, y, t) = 0.0, \quad p_x(4, y, t) = 0.0$$

On the lower boundary after the point $x = 1/6$, reflective wall boundary condition is imposed; and on the upper boundary the exact flow solution is imposed, i.e. the post-shock values Eqs. (5.5) for $x < 1/6 + \sqrt{3}(1 + 20t)$, and the pre-shock values Eqs. 5.6 for $x > 1/6 + \sqrt{3}(1 + 20t)$.

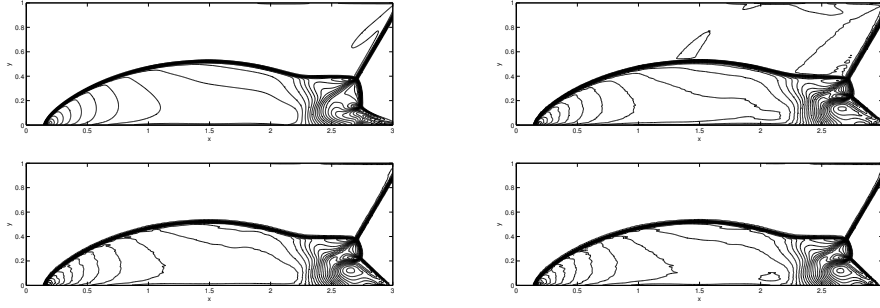


FIG. 5.19. Density at $T = 0.2$ calculated on: uniform mesh with $\phi^{van\ Albada}$ (upper-left); non-uniform mesh ($r = 0.3$) with first-order Godunov scheme (upper-right); non-uniform mesh ($r = 0.3$) with $\phi^{van\ Albada}$; non-uniform mesh ($r = 0.3$) with $\phi_{A,B}^{van\ Albada}$

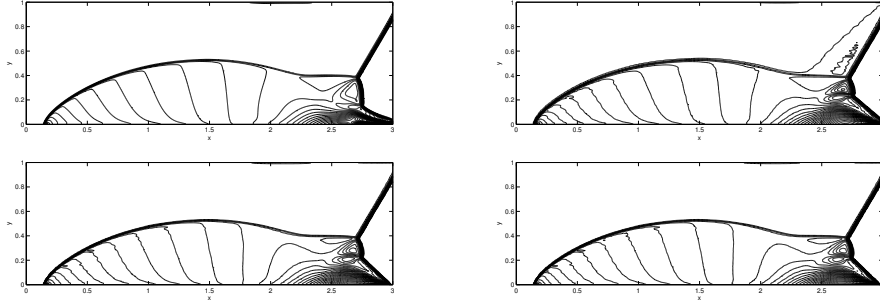


FIG. 5.20. Mach number at $T = 0.2$ calculated on: uniform mesh with $\phi^{van\ Albada}$ (upper-left); non-uniform mesh ($r = 0.3$) with first-order Godunov scheme (upper-right); non-uniform mesh ($r = 0.3$) with $\phi^{van\ Albada}$; non-uniform mesh ($r = 0.3$) with $\phi_{A,B}^{van\ Albada}$

The problem is solved to $T = 0.2$, and the numerical solutions in the domain $[0, 3] \times [0, 1]$ obtained from four simulations are presented in Figures 5.19–5.21. For all the simulations, the size of the mesh is 480×120 . The upper-left parts represent the solutions obtained from MUSCL with $\phi^{van\ Albada}$ on uniform grid. The other three simulations use non-uniform grids generated with $r = 0.3$: the upper-right parts are obtained from first-order Godunov scheme; the lower-left figures are computed using MUSCL with the conventional limiter $\phi^{van\ Albada}$; the lower-right contours are results using MUSCL with the enhanced limiter $\phi_{A,B}^{van\ Albada}$. It should be mentioned that the spatial resolution used here is not fine enough to resolve the fine structures, especially near the wave interaction sections; however the results showing here are sufficient for the comparison purpose.

It can be observed from the figures that

1. All simulations lead to stable results.
2. For this more challenging problem, the accuracy is mainly determined by the resolution of the meshes rather than the former order of the numerical schemes. However, one can still observe that the first scheme is less accurate, especially near the propagating shock fronts.
3. The structure in the shock reaction region computed from the uniform mesh is different from those obtained from the non-uniform mesh. This is mainly due to the fact that the three simulations use the same non-uniform meshes,

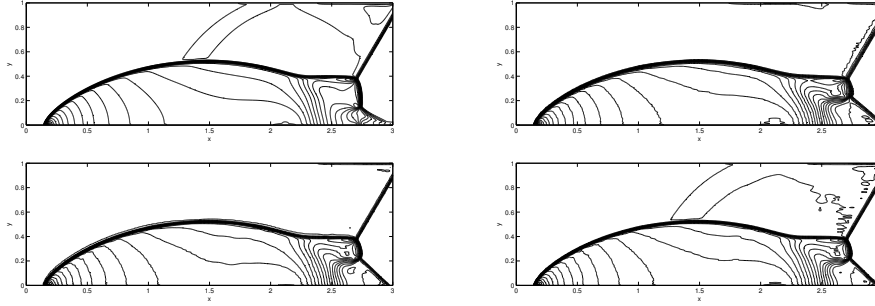


FIG. 5.21. Pressure at $T = 0.2$ calculated on: uniform mesh with $\phi^{van Albada}$ (upper-left); non-uniform mesh ($r = 0.3$) with first-order Godunov scheme (upper-right); non-uniform mesh ($r = 0.3$) with $\phi^{van Albada}$; non-uniform mesh ($r = 0.3$) with $\phi_{A,B}^{van Albada}$

which is consistent with the fact that the mesh is not fine enough to resolve the physical structure of the flow solutions.

5.3. Conclusions from the numerical examples. To summarize the numerical results

1. When the solution is smooth, enhanced limiters with MUSCL recover second-order convergence rates in space whereas conventional limiters only lead to first-order space accuracy. However, MUSCL with either enhanced or conventional limiters leads to more accurate solutions than the first order Godunov scheme.
2. For solutions that exhibit discontinuities, both conventional and enhanced limiters show similar stability property, which is consistent with the arguments before.
3. For very challenging problems like the double-Mach reflection problem, when the fine flow structure is under-resolved, the inaccuracy mainly comes from the mesh resolution rather than the formal order space accuracy of the numerical scheme. And for such problems, applying conventional limiters or enhanced limiters lead to visually similar solutions.

Especially, the last observation partially explains why it is hard to discover in practice that conventional limiters are inappropriate when applied on non-uniform meshes. However, this paper shows that by applying the enhanced limiters, which only needs minor modifications to the conventional ones, the accuracy in smooth regions can be greatly improved.

6. Conclusions. A general approach of studying and enhancing the limiters on non-uniform grids is presented. The theory presented follows the REP approach and Harten's stability theory, with modifications taking into account the non-uniform computational grids. The analysis is conducted for 1D problems, and it explains why formal second-order spatial accuracy is lost when conventional limiters are applied with non-uniform grids, and at the same time the TVD stability is retained. This study provides sufficient conditions for slope limiters on non-uniform meshes, so that TVD stability, formal second-order spatial accuracy and symmetry-preserving property are achieved in the resulting numerical schemes. The results extend naturally to multiple dimensions, provided that cell-centered finite volume methods are used. Several most widely used limiter functions, including the *van Leer* and *van Albada*

limiters, are enhanced to satisfy these conditions; in addition, the latter two retain their smoothness property in the enhanced form. The enhanced limiters are applied to solve both 1D and 2D benchmark problems to show that second-order spatial accuracy is indeed recovered on non-uniform meshes, and TVD stability is retained.

Acknowledgments. The author thanks the support by a Stanford Graduate Fellowship. The author also gratefully thanks Charbel Farhat for reviewing the manuscript and his insightful suggestions.

REFERENCES

- [1] TIMOTHY BARTH AND MARIO OHLBERGER, Finite volume methods: Foundation and analysis, in Encyclopedia of Computational Mechanics, Erwin Stein, René de Borst, and Thomas J. R. Hughes, eds., vol. 1, John Wiley & Sons, Ltd, 2004.
- [2] MARSHA BERGER, MICHAEL J. AFTOSMIS, AND SCOTT M. MURMAN, Analysis of slope limiters on irregular grids, in 43rd AIAA Aerospace Science Meeting, January 2005.
- [3] JAY P. BORIS AND DAVID L. BOOK, Flux-corrected transport. i. shasta, a fluid transport algorithm that works, J. Comput. Phys., 11 (1973), pp. 38–69.
- [4] PHILLIP COLELLA, A direct eulerian muscl scheme for gas dynamics, SIAM J. Sci. Comput., 6 (1985), pp. 104–117.
- [5] C. RICHARD DEVORE, Flux-corrected transport techniques for multidimensional compressible magnetohydrodynamics, J. Comput. Phys., 92 (1991), pp. 142–160.
- [6] S. K. GODUNOV, A difference scheme for numerical solution of discontinuous solution of hydrodynamic equations, Math. Sbornik, 47 (1959), pp. 271–306. also as US JPRS translation 7226 (1960).
- [7] JONATHAN B. GOODMAN AND RANDALL J. LEVEQUE, A geometric approach to high resolution tvd schemes, SIAM J. Numer. Anal., 25 (1988), pp. 268–284.
- [8] S. GOTTLIEB AND CHI-WANG SHU, Total variation diminishing runge-kutta schemes, Math. Comput., 67 (1998), pp. 73–85.
- [9] AMI HARTEN, High resolution schemes for hyperbolic conservation laws, J. Comput. Phys., 49 (1983), pp. 217–237.
- [10] M. E. HUBBARD, Multidimensional slope limiters for muscl-type finite volume schemes on unstructured grids, J. Comput. Phys., 155 (1999), pp. 54–74.
- [11] PETER LAX AND BURTON WENDROFF, Systems of conservation laws, Commun. Pure Appl. Math., 13 (1960), pp. 217–237.
- [12] RANDALL J. LEVEQUE, Finite Volume Methods for Hyperbolic Problems, Cambridge University Press, 1 ed., September 2002.
- [13] STANLEY OSHER, Convergence of generalized muscl schemes, SIAM J. Numer. Anal., 22 (1985), pp. 947–961.
- [14] P. L. ROE, Approximate riemann solvers, parameter vectors, and difference schemes, J. Comput. Phys., 43 (1981), pp. 357–372.
- [15] ———, Characteristic-based schemes for the euler equations, Ann. Rev. Fluid Mech., 18 (1986), pp. 337–365.
- [16] CHI-WANG SHU, High order finite difference and finite volume weno schemes and discontinuous galerkin methods for cfd, Int. J. Comput. Fluid Dyn., 17 (2003), pp. 107–118.
- [17] GARY A SOD, A survey of several finite difference methods for systems of nonlinear hyperbolic conservation laws, J. Comput. Phys., 27 (1978), pp. 1–31.
- [18] P. K. SWEBY, High resolution schemes using flux limiters for hyperbolic conservation laws, SIAM J. Numer. Anal., 21 (1984), pp. 995–1011.
- [19] G. D. VAN ALBADA, B. VAN LEER, AND W. W. ROBERTS JR., A comparative study of computational methods in cosmic gas dynamics, Astron. Astrophys., 108 (1982), pp. 76–84.
- [20] BRAM VAN LEER, Towards the ultimate conservative difference scheme i. the quest of monotonicity, Springer Lecture Notes in Physics, 18 (1973), pp. 163–168.
- [21] ———, Towards the ultimate conservative difference scheme ii. monotonicity and conservation combined in a second-order scheme, J. Comput. Phys., 14 (1974), pp. 361–370.
- [22] ———, Towards the ultimate conservative difference scheme iii. upstream-centered finite-difference schemes for ideal compressible flow, J. Comput. Phys., 23 (1977), pp. 263–275.
- [23] ———, Towards the ultimate conservative difference scheme v. a second-order sequel to godunov’s method, J. Comput. Phys., 32 (1979), pp. 101–136.

- [24] V. VENKATAKRISHNAN, Convergence to steady state solutions of the euler equations on unstructured grids with limiters, J. Comput. Phys., 118 (1995), pp. 120–130.
- [25] R. F. WARMING AND RICHARD M. BEAM, Upwind second-order difference schemes and applications in aerodynamic flows, AIAA Journal, 14 (1976), pp. 1241–1249.
- [26] P. WOODWARD AND P. COLELLA, The numerical simulation of two-dimensional fluid flow with strong shocks, J. Comput. Phys., 54 (1984), pp. 115–173.
- [27] STEVEN T. ZALESAK, Fully multidimensional flux-corrected transport algorithms for fluids, J. Comput. Phys., 31 (1979), pp. 335–362.

Appendix A. Measuring errors and computing convergence rates on non-uniform meshes. Given two randomly generated irregular meshes of the domain $[a, b]$, which are defined by the cell faces

$$\begin{aligned} \text{Mesh I: } a &= x_{1/2}^I < x_{3/2}^I < \cdots < x_{(N_1-1)+1/2}^I < x_{N_1+1/2}^I = b \\ \text{Mesh II: } a &= x_{1/2}^{II} < x_{3/2}^{II} < \cdots < x_{(N_2-1)+1/2}^{II} < x_{N_2+1/2}^{II} = b \end{aligned}$$

The reference cell-sizes for the two meshes are $h^I = (b - a)/N_1$ and $h^{II} = (b - a)/N_2$ respectively.

For generic variable u to be solved for, define u_i^I and u_i^{II} as the numerical solutions computed by the same scheme on the two meshes respectively at a given terminal time T . In addition, define $u^{ref}(x, T)$ as the reference solution at location x and terminal time T is available either from analytical solution or from numerical solution computed on a much finer grids. The L_1 norm of the computed errors are hence calculated as

$$\begin{aligned} E^I &= \sum_{i=1}^{N_1} (x_{i+1/2}^I - x_{i-1/2}^I) |u_i^I - u^{ref}(x_i^I, T)| \\ E^{II} &= \sum_{i=1}^{N_2} (x_{i+1/2}^{II} - x_{i-1/2}^{II}) |u_i^{II} - u^{ref}(x_i^{II}, T)| \end{aligned}$$

Then the convergence rates is estimated by

$$R = \frac{\log(E^I) - \log(E^{II})}{\log(h^I) - \log(h^{II})} \quad (\text{A.1})$$

Note that the equation above is widely used for estimating convergence rates on uniform meshes, and its validity for the same purpose on non-uniform meshes is open for discussion. However the numerical results presented in Section 5 justifies this choice for irregular meshes generated in the way described in Section 2.

Appendix B. Effect of alternative smoothness monitors on the *van Leer* limiter. An alternative strategy to deal with the issues raised in this paper is to choose different smoothness monitors from that given by Eq. (2.11), while still using conventional limiter functions. These smoothness monitors could be designed to account for non-uniform meshes, like

$$\theta_i^{alt} = \frac{\frac{u_i - u_{i-1}}{x_i - x_{i-1}}}{\frac{u_{i+1} - u_i}{x_{i+1} - x_i}} = \frac{\Delta x_i + \Delta x_{i+1}}{\Delta x_{i-1} + \Delta x_i} \cdot \frac{u_i - u_{i-1}}{u_{i+1} - u_i} = \frac{\Delta x_i + \Delta x_{i+1}}{\Delta x_{i-1} + \Delta x_i} \theta_i \quad (\text{B.1})$$

and accordingly the limited slope σ_i^n is

$$\sigma_i^{n,alt} = \phi(\theta_i^{alt}) \cdot \frac{u_{i+1}^n - u_i^n}{x_{i+1} - x_i} = \phi(\theta_i^{alt}) \cdot \frac{2(u_{i+1}^n - u_i^n)}{\Delta x_i + \Delta x_{i+1}} \quad (\text{B.2})$$

Using these alternatives with the conventional *minmod*, *superbee* and *MC* limiters, the effect is the same as the enhancement proposed in this paper. On the other hand, the same does not necessarily hold for general slope limiters. For example, see the following result concerning the *van Leer* limiter and a large range of smoothness monitors.

THEOREM B.1. *Supposing any alternative smoothness monitor and limited slopes given by the following*

$$\theta_i^{alt} = \alpha_i \theta_i^p \quad (\text{B.3})$$

$$\sigma_i^{n,alt} = \phi_i^{van\ Leer} (\theta_i^{alt}) \beta_i \theta_i^q \frac{u_{i+1}^n - u_i^n}{\Delta x_i} \quad (\text{B.4})$$

where θ_i is defined by Eq. (2.11). α_i and β_i are positive constants that only rely on the grid information; and $p \in \{\pm 1\}$, $q \in \{0, 1\}$. Eqs. (B.3–B.4) are equivalent to

$$\sigma_i^{n,alt} = \phi_i^{van\ Leer} \frac{u_{i+1}^n - u_i^n}{\Delta x_i}$$

where

$$\phi_i^{van\ Leer} = \beta_i \theta_i^q \phi_i^{van\ Leer} (\alpha_i \theta_i^p) \quad (\text{B.5})$$

Then the equivalent limiter $\phi_i^{van\ Leer}$ cannot satisfy both the order condition (3.21) and the TVD stability condition (3.11) for arbitrary non-uniform grids.

Before going to the proof of this theorem, the two parameters p and q is motivated from the following

$$\theta_i^{-1} = \frac{u_{i+1}^n - u_i^n}{u_i^n - u_{i-1}^n}, \quad \theta_i(u_{i+1}^n - u_i^n) = u_i^n - u_{i-1}^n$$

Thus by introducing p and q in Eqs. (B.3–B.4), Theorem B.1 covers a large range of possible smoothness monitors and reconstructed slopes.

Proof. [Proof of Theorem B.1] Suppose $\theta_i > 0$ in the following proof. The equivalent limiter given by Eq. (B.5) has the following explicit expression

$$\phi_i^{van\ Leer} = \frac{2\alpha_i \beta_i \theta^{p+q}}{1 + \alpha_i \theta^p}$$

Noting $p = \pm 1$ and $q = 0, 1$, the formula above can be simplified as

$$\phi_i^{van\ Leer} = \frac{\theta^t}{a + b\theta}, \quad t = 1, 2$$

where a and b are positive constants that are determined by α_i , β_i and p . Define the grid parameters $A = \frac{\Delta x_{i-1} + \Delta x_i}{\Delta x_i + \Delta x_{i+1}}$ and $B = \frac{2\Delta x_i}{\Delta x_i + \Delta x_{i+1}}$. Thus it is sufficient to proof that one cannot choose a and b as functions of A and B , such that the following two conditions hold for all $\theta > 0$, and all possible pair (A, B) .

$$0 \leq \frac{\theta^t}{a + b\theta} \leq 2 \min(1, \theta) \quad (\text{B.6})$$

and also

$$\frac{A^t}{a + bA} = B \quad (\text{B.7})$$

First consider Eq. (B.6), one obtains

$$\frac{\theta^t}{a + b\theta} \leq 2, \forall \theta > 0 \quad \Rightarrow \quad t = 1, 2b \geq 1$$

Applying $t = 1$, it follows again from Eq. (B.6) that

$$\frac{\theta}{a + b\theta} \leq 2\theta, \forall \theta > 0 \quad \Rightarrow \quad 2a \geq 1$$

Next consider Eq. (B.7), by applying $t = 1$, it leads to

$$2a + 2bA = \frac{2A}{B}$$

Thus if both Eq. (B.6) and Eq. (B.7) hold, one must have

$$\frac{2A}{B} \geq 1 + A, \quad \forall A, B, \text{ s.t. } 0 \leq B < 2 \min(1, A)$$

which is, however, not true. \square